Published in final edited form as:
J Magn Reson Imaging. 2013 February ; 37(2): 313–331. doi:10.1002/jmri.23844.

Hyperpolarized ^{129}Xe MRI of the Human Lung

John P. Mugler III, Ph.D.[1] and **Talissa A. Altes, M.D.**[1]

[1]Center for In-vivo Hyperpolarized Gas MR Imaging, Department of Radiology and Medical Imaging, University of Virginia School of Medicine, Charlottesville, VA, USA

Abstract

By permitting direct visualization of the airspaces of the lung, MR imaging using hyperpolarized gases provides unique strategies for evaluating pulmonary structure and function. Although the vast majority of research in humans has been performed using hyperpolarized ^{3}He, recent contraction in the supply of ^{3}He and consequent increases in price have turned attention to the alternative agent, hyperpolarized ^{129}Xe. Compared to ^{3}He, ^{129}Xe yields reduced signal due to its smaller magnetic moment. Nonetheless, taking advantage of advances in gas-polarization technology, recent studies in humans using techniques for measuring ventilation, diffusion, and partial pressure of oxygen have demonstrated results for hyperpolarized ^{129}Xe comparable to those previously demonstrated using hyperpolarized ^{3}He. In addition, xenon has the advantage of readily dissolving in lung tissue and blood following inhalation, which makes hyperpolarized ^{129}Xe particularly attractive for exploring certain characteristics of lung function, such as gas exchange and uptake, which cannot be accessed using ^{3}He. Preliminary results from methods for imaging ^{129}Xe dissolved in the human lung suggest that these approaches will provide new opportunities for quantifying relationships among gas delivery, exchange, and transport, and thus show substantial potential to broaden our understanding of lung disease. Finally, recent changes in the commercial landscape of the hyperpolarized-gas field now make it possible for this innovative technology to move beyond the research lab.

Keywords

Hyperpolarized gas; lung imaging; pulmonary disease; xenon-129; helium-3

Clinical magnetic resonance imaging (MRI) of the lung is challenging due to the lung's low proton density, which is roughly one-third that of muscle (1), and the inhomogeneous magnetic environment within the lung created by numerous air-tissue interfaces, which lead to a T2* value on the order of 1 ms at 1.5T (1,2). Although advances continue with techniques such as ultrashort echo time (UTE) imaging of the lung parenchyma (3), conventional proton-based MRI is at a fundamental disadvantage for pulmonary applications because it cannot directly image the lung airspaces. This disadvantage of proton MRI can be overcome by turning to a gaseous contrast agent, such as the noble gas helium-3 (^{3}He) or xenon-129 (^{129}Xe), which upon inhalation permits direct visualization of lung airspaces in an MR image (4–8). With these agents, the low density of gas compared to that of solid tissue can be compensated by using a standalone, laser-based polarization device (9,10) to increase the nuclear polarization to be roughly five orders of magnitude (10,000 times) higher than the corresponding thermal equilibrium polarization would be in the magnet of a clinical MR scanner. As a result, the MR signal from these *hyperpolarized* noble gases is increased by a proportionate amount and is easily detected using an MR scanner tuned to the

Corresponding author: John P. Mugler, III, Ph.D., University of Virginia, P.O. Box 801339, Charlottesville, VA 22908, John.Mugler@virginia.edu.

appropriate resonance frequency. MRI using hyperpolarized gases has led to the development of numerous unique strategies for evaluating the structure and function of the human lung (4–8) which provide advantages relative to current clinically-available methods. For example, as compared with nuclear-medicine ventilation scintigraphy scans using ^{133}Xe or aerosolized technetium-99m DTPA, hyperpolarized-gas ventilation MR images provide improved temporal and spatial resolution, expose the patient to no ionizing radiation, and can be repeated multiple times in a single day if desired. Although inhaled xenon has also been used as a contrast agent with computed tomography (CT), which can provide high spatial and temporal resolution, the high radiation dose and low contrast on the resulting ventilation images has dampened enthusiasm for the CT-based technique.

Although the first hyperpolarized-gas MR images were obtained using hyperpolarized ^{129}Xe (11), and images of the human lung were acquired with hyperpolarized ^{129}Xe only a few years later (12), the vast majority of work in humans has been performed using hyperpolarized ^{3}He instead. This occurred primarily because ^{3}He provided a stronger MR signal, due to its larger nuclear magnetic moment (and hence larger gyromagnetic ratio) compared to ^{129}Xe and historically high levels of polarization (greater than 30%) achieved for ^{3}He, and because there are no significant safety concerns associated with inhaled helium. However, in the years following the terrorist attacks of 9/11, there was a surge in demand for ^{3}He for use in neutron detectors for port and border security, and this demand far exceeded the replenishment rate from the primary source, the decay of tritium used in nuclear warheads (13,14). As a result, ^{3}He prices skyrocketed and availability plummeted. Currently, the U.S. government is regulating the supply of ^{3}He, allocating this precious resource among users whose research or applications depend on ^{3}He's unique physical properties (15). This includes an annual allocation for medical imaging, which allows research on hyperpolarized ^{3}He MRI of the lung to continue. Nonetheless, unless a new source for ^{3}He is found, it is clear that insufficient ^{3}He is available to permit hyperpolarized ^{3}He MRI of the lung to translate from the research community to a clinical tool.

In contrast to ^{3}He, ^{129}Xe is naturally abundant on Earth and its cost is relatively low. Thus, ^{129}Xe is the obvious potential alternative to ^{3}He as an inhaled contrast agent for MRI of the lung. While the ^{3}He availability crisis has accelerated efforts to develop and evaluate hyperpolarized ^{129}Xe for human applications, it is important to understand that ^{129}Xe is not just a lower-signal alternative to ^{3}He, forced upon us by practical necessity. In particular, the relatively high solubility of xenon in biological tissues (16) and an exquisite sensitivity to its environment, which results in an enormous range of chemical shifts upon solution (17), make hyperpolarized ^{129}Xe particularly attractive for exploring certain characteristics of lung function, such as gas exchange and uptake (18–27), that cannot be accessed using hyperpolarized ^{3}He. The quantitative characteristics of gas exchange and uptake are determined by parameters of physiologic relevance, including the thickness of the blood-gas barrier (23), and thus measurements that quantify this process offer a potential wealth of information on the functional status of the healthy and diseased lung.

Historically, polarization levels for liter-quantities of hyperpolarized ^{129}Xe have been roughly 10%, while those for similar quantities of hyperpolarized ^{3}He have been greater than 30%. (Recall that the thermal-equilibrium polarization of water protons at 1.5T is 0.0005% -- four to five orders of magnitude lower.) Given ^{129}Xe's lower nuclear magnetic moment, this situation has put hyperpolarized ^{129}Xe at a distinct disadvantage relative to ^{3}He. A recent, key advance for ^{129}Xe is the development of systems that can deliver liter quantities of hyperpolarized ^{129}Xe with polarization on the order 50% (28). This now puts ^{129}Xe on competitive footing with ^{3}He, positioning MRI of the human lung using hyperpolarized ^{129}Xe to advance quickly in the immediate future, and making

hyperpolarized ^{129}Xe MRI of interest to the broader Radiology and medical-imaging communities.

After laying the technical foundation for hyperpolarized-gas MRI in the following three sections, we review the current state of the art for hyperpolarized ^{129}Xe MRI of the human lung, including methods for visualizing and quantifying the lung airspaces, as well as those for measuring gas exchange and uptake. Considering the important role that ^{3}He has played in the development of hyperpolarized-gas MRI of the lung, several aspects of our discussion of ^{129}Xe will be presented in the context of ^{3}He. We conclude with a discussion of important issues related to the potential translation of hyperpolarized ^{129}Xe MRI to the clinical realm. Readers interested principally in the imaging results that can be obtained using hyperpolarized ^{129}Xe may skip the sections on *Gas Polarization* and *Pulse Sequences* with only minor loss of continuity.

PROPERTIES OF ^{129}Xe

Of the nine stable isotopes of xenon, ^{129}Xe is of particular interest for MRI because it has a nuclear spin of ½, just like protons in water or fat molecules, and is not radioactive. However, in contrast to protons in water or fat, the net nuclear spin for ^{129}Xe arises from an unpaired neutron. MRI-relevant properties for ^{129}Xe gas, compared to those for ^{3}He gas and protons in water, are presented in Table 1. We see that 26% of naturally occurring xenon is ^{129}Xe, while the natural abundance of ^{3}He is negligible. (This is why ^{3}He used for medical imaging has been obtained from the decay of tritium, as discussed above.) Currently, isotopically-enriched xenon gas (~80% ^{129}Xe) can be purchased for ~100 USD per liter. Until a few years ago, ^{3}He could be purchased for roughly the same amount, but now the cost is about an order of magnitude higher, and supplies are very limited.

For magnetic field strengths commonly used in clinical MRI (1.5T and above), the thermal noise in the image arises largely from the patient, as opposed to the radio-frequency (RF) coil. For this situation, it is straightforward to show that the signal-to-noise ratio (SNR) for hyperpolarized-gas MRI is directly proportional to the gyromagnetic ratio, and unlike conventional proton-based MRI does not vary substantially with field strength (29–31). Thus, considering equal amounts of pure ^{129}Xe and ^{3}He with the same polarization, comparison of the gyromagnetic ratios for the two gases (Table 1) indicates that ^{3}He would have a substantial (~3-fold) SNR advantage over ^{129}Xe. Depending on imaging parameters, however, the lower diffusion coefficient and lower gyromagnetic ratio (and thus lower resonance frequency) of ^{129}Xe may act in its favor. For example, the lower diffusion coefficient would yield less signal attenuation for high-resolution imaging, and the lower gyromagnetic ratio would result in decreased dephasing due to off-resonance effects, such as from magnetic-susceptibility interfaces. Even so, to maximize the utility of ^{129}Xe in light of its relatively low gyromagnetic ratio, it is important to achieve relatively high polarization levels (as noted above), to use isotopically-enriched xenon (since the signal varies directly with the fraction of ^{129}Xe), and to use state-of-the-art RF-coil technology (32–35).

As a gas, the diffusion coefficient for ^{129}Xe is several orders of magnitude larger than that for water in biological tissues. This situation has both positive and negative consequences. On one hand, even the standard spatial-encoding gradients can lead to substantial diffusion-induced attenuation of the MR signal. This factor can limit spatial resolution and SNR in hyperpolarized-gas images, and is thus important to consider when designing the associated pulse sequences. On the other hand, the high diffusion coefficient permits diffusion-weighted imaging of hyperpolarized gases to be used for quantitatively characterizing the microstructure of the lung. Both of these issues are discussed in more detail later in this article.

Finally, as indicated in Table 1, xenon gas is soluble in a variety of substances, while helium gas in general has very low solubility (16). In particular, xenon is lipophilic, having a high solubility in oils and lipid-containing tissues. As mentioned above, these solubility characteristics, combined with the associated large chemical shifts, make ^{129}Xe a valuable probe for exploring gas exchange and uptake in the lung. Nonetheless, for human applications, xenon presents the complication of being a general anesthetic at high concentrations (> 70%). However, with appropriate dosing procedures, hyperpolarized ^{129}Xe can be used for lung MRI with only minor, transient side effects such as dizziness or mild euphoria (36); no significant adverse events were observed by either Patz et al (25) or Driehuys et al (37) in studies including both healthy subjects and subjects with lung disease. For years, isotopes of xenon have been used in humans for xenon-enhanced CT and nuclear-medicine studies. At current levels of polarization, the typical adult dose of ^{129}Xe for hyperpolarized-gas MRI is 0.5–1 L. The total xenon dose is much lower for nuclear-medicine ventilation scintigraphy, but much greater for xenon-enhanced CT.

GAS POLARIZATION

Although it is possible to image either ^{129}Xe or ^{3}He by simply placing the gas (in a suitable container) in the magnet of an MR scanner, the low density of gas compared to that of solid tissue results in a signal that is too low to be of practical use for imaging the human lung. (Samples of ^{129}Xe or ^{3}He pressurized to several atmospheres to obtain high gas density are, however, useful for testing and quality-control purposes.) Nonetheless, the nuclear polarization can be increased dramatically compared to that produced by the magnet of the MR scanner by using a method called optical pumping and spin exchange (OPSE) (9,38), which was originally developed for nuclear-physics experiments many years before being applied to medical imaging.

As its name implies, OPSE is, in concept, a two-step process. The first step, *optical pumping*, involves using a laser to generate electron-spin polarization in a vapor of an alkali metal. This process takes place within a glass container, called an optical cell (Fig 1a; Fig. 1b, top center), positioned within a magnetic field (Fig. 1a; Fig. 1b, top right). A small amount of the alkali metal, typically rubidium, is placed in the cell, which is heated (Fig. 1b, top right) during the polarization process to create rubidium vapor. The optical cell is illuminated with circularly-polarized laser light (Fig. 1a, left; Fig. 1b, center) at a specific wavelength (795 nm) to optically *pump* the rubidium atoms. This pumping preferentially populates one of the two spin states for the valence electron, thereby polarizing the associated electron spins and resulting in electron-spin polarization approaching 100%. In the second step of OPSE, collisions between spin-polarized rubidium atoms and noble-gas (^{129}Xe or ^{3}He) atoms within the cell result in *spin exchange* -- the transfer of polarization from rubidium electrons to noble-gas nuclei (Fig. 1a, right). After spin-exchange collisions, rubidium atoms absorb additional laser light to repolarize their electrons. The spin-exchange process then continues through additional collisions, increasing the nuclear polarization of the noble gas. It is important to note that a collision can also depolarize the rubidium valence electron without polarizing the noble-gas nucleus. Competition between these undesired (electron-spin destruction) collisions and the desired (spin-exchange) collisions limits efficiency of the process.

While the basic OPSE process described above is effective for generating high polarization in a “batch” of pressurized ^{3}He over a period of several hours, the situation is somewhat more complicated for ^{129}Xe. The efficiency of both the desired and undesired rubidium-noble-gas collisions is substantially higher for ^{129}Xe than for ^{3}He. The positive aspect of this is that the maximum ^{129}Xe polarization is reached rapidly (in seconds), while the

negative aspect is that any significant concentration of ^{129}Xe in the optical cell leads to low rubidium polarization through electron-spin destruction collisions, which severely limits the attainable ^{129}Xe polarization. To overcome this difficulty, Driehuys et al (10) developed an alternative to the batch approach wherein a gas mixture containing a low fraction of ^{129}Xe (on the order of a percent) flows continuously through the optical cell, such that any given ^{129}Xe atom spends a few seconds in the cell -- sufficient time to achieve high nuclear polarization -- and the low concentration of ^{129}Xe limits electron-spin destruction collisions, allowing reasonable rubidium electron-spin polarization to be maintained. After the polarized ^{129}Xe gas mixture exits the optical cell, it flows through a cryogenic accumulator ("cold finger") bathed in liquid nitrogen, which freezes ^{129}Xe out of the gas mixture and stores it until the desired amount of hyperpolarized ^{129}Xe is obtained. Then, the frozen ^{129}Xe is thawed and transferred to a plastic dosing bag (Fig. 1, top left) for administration to the subject. Over the past several years, Hersman and colleagues (28) have optimized the design of a ^{129}Xe polarization system based on the flowing approach to achieve delivered polarizations approaching 50% for liter quantities of hyperpolarized ^{129}Xe.

PRACTICAL CONSIDERATIONS

Hardware

Compared to the requirements for routine proton MRI, several additional pieces of hardware are necessary to perform hyperpolarized-gas MRI. First and foremost, a system for polarizing the gas -- a *polarizer* -- is needed. Figure 1 shows an early commercial prototype of a polarizer that includes an exchangeable central "cartridge," which permits the system to be used for either ^{129}Xe or ^{3}He gases. This system, manufactured in 1996, has been used routinely at our institution over the past 15 years, and can produce ~0.5 liter of ^{129}Xe polarized to 5–10%. Figure 2 shows a commercial prototype of a new system designed specifically for ^{129}Xe. This polarizer uses a low-pressure, high-velocity, counter-flow spin-exchange column (Fig. 2, right) to improve efficiency of the polarization process compared to earlier designs (28,39). In preliminary tests at our institution, this system has routinely delivered ~2-liter batches of hyperpolarized ^{129}Xe with polarizations of 30–50%.

Since the gyromagnetic ratio for ^{129}Xe is different than that for protons (Table 1), the MR scanner must be modified to operate at the associated resonance frequency, which for ^{129}Xe at 1.5T is approximately 17.7 Mhz, compared to 63.9 MHz for protons. Typically, the primary hardware addition is a second RF-power amplifier that supports additional frequencies, but, depending on the manufacturer, a package for multinuclear imaging may also include additional receiver hardware, specialized pulse sequences, or other minor hardware modifications.

Lastly, a dedicated RF coil is needed to permit imaging at the ^{129}Xe resonance frequency. To date, RF coils for hyperpolarized gases have not been available from scanner manufacturers, and thus many researcher groups have built their own custom RF coils (32–35). Nonetheless, several of the third-party MR-device manufacturers offer RF coils for ^{129}Xe or ^{3}He imaging, including multi-coil array configurations. At our institution, we currently use chest RF coils from three different third-party manufacturers (Clinical MR Solutions, Brookfield, WI; Medical Engineering & Technology, Princeton, NJ; and Rapid Biomedical, Rimpar, Germany), as well as custom RF coils built in-house.

Pulse Sequences

The naturally high diffusion coefficients of gases and the non-equilibrium nature of hyperpolarized magnetization lead to unique considerations for the design of pulse sequences for hyperpolarized-gas MRI of the lung. Although the details of these design

considerations are beyond the scope of this article, some general observations may be helpful to the reader.

Diffusion-induced attenuation of the MR signal depends on the product of the so-called *b value* for the associated gradient waveform (including any intervening time delays), which characterizes the amount of diffusion-induced attenuation imparted by the gradient waveform, and the diffusion coefficient for the substance of interest. Signal attenuation increases as either the *b* value or diffusion coefficient increases, and the *b* value increases as either the strength or duration of the associated gradient waveform increases. Due to the relatively small diffusion coefficient for water molecules in tissue, very large (i.e., high gradient strength and long duration) gradient pulses must be added to most pulse sequences used in proton MRI to obtain substantial attenuation of the MR signal due to diffusion. For example, in diffusion-weighted proton MRI based on single-shot echo-planar imaging, the gradient pulses added to the pulse sequence to achieve diffusion sensitization are typically tens of milliseconds long and use gradient strengths approaching the maximum for the scanner. In contrast, for hyperpolarized-gas MRI, the high diffusion coefficient of the gases can result in substantial diffusion-induced signal attenuation from just the standard imaging gradients, without addition of specific diffusion-sensitization gradient pulses. Thus, pulse sequences for which transverse magnetization generated by a given excitation RF pulse experiences substantial gradient activity, as in fast/turbo spin-echo imaging, are of limited utility for hyperpolarized-gas MRI because diffusion-induced signal attenuation is quite high unless the spatial resolution is low (40,41). As a result, echo-train-based pulse sequences such as fast/turbo spin echo or single-shot echo-planar imaging are not widely used for hyperpolarized-gas MRI of the lung.

In proton MRI, recovery of the longitudinal component of the magnetization through T1 relaxation is fundamental to the design of most pulse sequences. Regrowth of longitudinal magnetization during the time between repetitions of the RF pulse(s) associated with a given slice (that is, TR) is necessary to obtain adequate signal levels in the images. In contrast, because hyperpolarized magnetization is not at thermal equilibrium in the static magnetic field of the MR scanner, and because it is many times larger than the thermal equilibrium magnetization, T1 relaxation results in decay, not regrowth, of longitudinal magnetization.

This important difference between thermally-polarized and hyperpolarized magnetization is illustrated in Fig. 3, which shows the temporal evolution of the longitudinal component of the magnetization for either thermally-polarized or hyperpolarized magnetization subject to two common pulse sequences. The plot on the upper left shows the familiar situation for thermally-polarized magnetization and a single spin-echo pulse sequence. The longitudinal magnetization starts at its thermal equilibrium value (M_o), becomes zero as the first 90° excitation RF pulse is applied at time zero, and then relaxes to an intermediate value determined by the TR of the pulse sequence and T1 of the tissue. As the pulse sequence repeats, the longitudinal magnetization again becomes zero as each successive 90° excitation RF pulse is applied (at multiples of 0.5 s for this example), and relaxes back to the same value between RF pulses. In contrast, as illustrated in the upper-right plot, the hyperpolarized longitudinal magnetization does not relax back to its initial value (M_h) following the first 90° excitation RF pulse applied at time zero. Instead, it remains zero. (Actually, the hyperpolarized magnetization does relax back to M_o for the gas, but, because M_o is so small compared to M_h, the value is zero for practical purposes.) Following a 90° excitation RF pulse, additional hyperpolarized gas would need to be administered to regain a useable level of magnetization. Since hyperpolarized-gas MR images of the human lung are generally obtained using a single inhalation of gas, pulses sequences that require repeated high-flip-angle excitation RF pulses, such as conventional spin-echo or fast/turbo spin-echo, are generally not useful.

Given that the total magnetization available following an inhalation of hyperpolarized gas is fixed, an effective approach is to use a pulse sequence that consumes only a small fraction of the longitudinal magnetization each repetition -- low-flip-angle gradient-echo imaging. For thermally-polarized magnetization, the longitudinal component begins at M_o and gradually approaches a steady-state level as the fraction of longitudinal magnetization used by each RF pulse is balanced by regrowth of the magnetization between RF pulses (Fig. 3, lower-left plot). Since analogous recovery of the longitudinal magnetization does not occur for hyperpolarized gas, it is fortunate that the T1 relaxation time is quite long (~20 s for hyperpolarized ^{129}Xe in the lung), and thus, over a period of several seconds, loss of magnetization from T1 decay is not substantial. As a result, although the longitudinal component of hyperpolarized magnetization decreases monotonically as RF pulses are applied during the low-flip-angle gradient-echo acquisition (Fig. 3, lower-right plot), appropriate choice of the flip-angle value provides relative levels of longitudinal magnetization that are similar to those for thermally-polarized magnetization (compare lower-left and lower-right plots of Fig. 3). Because of this favorable behavior for low-flip-angle gradient-echo pulse sequences, they form the basis for the majority of techniques used for hyperpolarized-gas MRI of the lung.

For standard sequential phase encoding, wherein the center of *k* space is acquired midway through the acquisition, it is easy to show that an optimum flip angle exists which provides the highest SNR for a hyperpolarized-gas acquisition (42). An interesting consequence of having fixed total longitudinal magnetization available for a gradient-echo acquisition is that the SNR is independent of the number of phase-encoding steps (aside from a relatively weak dependence on the long T1) when the optimum flip angle is used (42). This behavior has important consequences for parallel imaging with hyperpolarized gases; for an ideally-behaved RF-coil array, a hyperpolarized-gas gradient-echo acquisition can be accelerated without loss of SNR (32,43). For certain applications, further optimization of the gradient-echo acquisition, such as variable-flip-angle RF pulses or centric phase encoding, may be useful; these topics are discussed in refs. (44–47).

FUNCTION & STRUCTURE OF THE LUNG AIRSPACES

Over the past fifteen years, a number of techniques for characterizing the function and structure of the lung airspaces have been pioneered using hyperpolarized ^{3}He (4–8). Recently, translation of these techniques to hyperpolarized ^{129}Xe imaging in humans has begun (25,26,36,48–51). In the next few sections, we describe progress to date with ^{129}Xe in the historical context of ^{3}He.

Ventilation

The most commonly-used technique for hyperpolarized-gas MRI of the lung is *ventilation* imaging, which is performed by acquiring a series of two-dimensional images, or a three-dimensional image set, during a breath-hold period following inhalation of the gas. While ventilation images show high signal in normally-functioning regions of the lung, ventilation *defects* -- regions of absent or relatively low signal -- are seen in regions where airflow is partially or totally obstructed (52,53). Results from hyperpolarized ^{3}He imaging have shown that ventilation imaging is useful for detecting functional abnormalities in obstructive lung diseases, such as chronic obstructive pulmonary disease (COPD), cystic fibrosis and asthma (53–56). In terms of conventional proton-based MRI, ventilation imaging is simply spin-density-weighted imaging. Based on our discussion above concerning the non-equilibrium nature of the hyperpolarized magnetization, we can see that ventilation images will also be weighted by any variations in the value of the flip angle, or in the value of T1, among regions of the lung. Nonetheless, these effects are typically small for an appropriately designed acquisition. It is also important to note that single breath-hold imaging does not

measure quantitative (specific) ventilation in the context of respiratory physiology. Nonetheless, approaches to quantitatively evaluate ventilation have been developed based on ^{3}He imaging, and applied primarily in animal models (57–59); preliminary results in humans have also been reported (60,61).

In considering the translation of ventilation imaging from ^{3}He to ^{129}Xe, it is important to note that the physical properties of these two gases are very different: ^{3}He is a very small atom, lighter than the primary constituents of air, whereas ^{129}Xe is a rather large atom, much heavier than the primary constituents of air. These substantial disparities may manifest as differences in flow and distribution characteristics between the gases upon inhalation (62). Therefore, we cannot assume that the appearance of obstructive lung diseases in ^{129}Xe ventilation images will be identical to that in ^{3}He ventilation images. This is not to say ^{129}Xe may be inferior; the different physical characteristics of ^{129}Xe compared to ^{3}He could in fact make ^{129}Xe more sensitive for the detection of mild obstruction. Nonetheless, the following examples illustrate that the appearance of ventilation images acquired using ^{129}Xe are, at a minimum, very similar to those acquired using ^{3}He.

The quality of ventilation images that can currently be obtained in healthy subjects using hyperpolarized ^{129}Xe is illustrated in Fig. 4 (lower row), and compared to typical results from ^{3}He (middle row) and the first results obtained in humans using ^{129}Xe (top row) (12). The tremendous improvement in the quality of ^{129}Xe images since 1996 is attributable primarily to an increase in gas polarization; the polarization levels for the images in the top and bottom rows of Fig. 4 were approximately 1% and 35%, respectively. The ^{3}He images (middle row) show the typical quality that can be achieved using 300–400 ml of ^{3}He polarized to 30–40%. Despite the fact that the gyromagnetic ratio for ^{129}Xe is lower than that for ^{3}He as discussed above, similar image quality can be obtained for ^{129}Xe images (lower row) by using a larger dose of gas (~700 ml) and a multi-channel array RF coil (33). These ventilation images illustrate that ^{129}Xe distributes generally uniformly throughout the healthy lung, yielding results in healthy subjects which appear essentially the same as those from ^{3}He.

Ventilation defects associated with functional abnormalities from pulmonary disease are also clearly depicted with ^{129}Xe (48), as illustrated in Fig. 5 for subjects with asthma (upper row), COPD (middle row) or cystic fibrosis (lower row). These images show numerous ventilation defects secondary to disease, which are, at least qualitatively, similar to defects seen in ^{3}He images. A direct comparison between ^{129}Xe and ^{3}He images for two subjects with cystic fibrosis is shown in Fig. 6. For subject A (upper row), the ventilation defects appear essentially identical in the ^{129}Xe and ^{3}He images, whereas for subject B (lower row; same subject as shown in the lower row of Fig. 5), the ventilation defects in the ^{129}Xe images appear generally more severe than those in the ^{3}He images. Based on ^{129}Xe ventilation imaging of the lung performed one year earlier in subject A, the major ventilation defects are stable, suggesting complete airflow obstruction to the affected regions. Previous lung imaging was not performed in subject B. Nonetheless, one could speculate that at least some of the ventilation defects in this subject are associated with partial obstruction and that the heavier ^{129}Xe gas did not pass as easily through these partial obstructions, suggesting a higher sensitivity for ^{129}Xe to such obstructions. Anecdotal evidence aside, additional research is obviously needed to quantitatively evaluate any differences between ^{129}Xe and ^{3}He in depicting functional abnormalities from diseases such as asthma, COPD and cystic fibrosis.

Diffusion

The application of diffusion MRI techniques to hyperpolarized gases permits quantitative evaluation of the characteristics of the lung microstructure. Analogous to the information on

the microscopic motion of water molecules in tissue provided by diffusion-based methods used in proton MRI, diffusion-weighted hyperpolarized-gas MRI methods provide a measurement that reflects the random Brownian motion of the gas atoms within the airspaces of the lung (as opposed to the transmembrane diffusion of the gas, as measured with diffusing capacity of the lung for carbon monoxide [DLCO]) and the degree to which this random motion is restricted by the structure of lung tissue. As discussed above, diffusion results in attenuation of the MRI signal, and the degree of signal attenuation depends on the *b* value of the associated gradient waveform(s). (Although the standard imaging gradients can result in measureable signal attenuation from diffusion for hyperpolarized gases, as described above, diffusion-weighted methods use additional diffusion-sensitization gradients to impart a chosen degree of diffusion-induced signal attenuation.) By measuring the signal attenuation for at least 2 *b* values, an apparent diffusion coefficient (ADC), which varies inversely with the degree to which the diffusion of the gas is restricted in the lung, can be calculated. For example, the ADC for hyperpolarized gas in healthy lung parenchyma (~0.2 cm^2/s [^{3}He] or ~0.04 cm^2/s [^{129}Xe] for typical measurements using a maximum *b* value of 1.6 s/cm^2 [^{3}He] or 10 s/cm^2 [^{129}Xe]) is substantially smaller than the corresponding diffusion coefficient of the gas in an unrestricted space (~0.86 cm^2/s [^{3}He] or ~0.14 cm^2/s [^{129}Xe] for the dilute gas in air [Table 1]). Further, the ADC measured in a lung with severe emphysema is larger than that for a healthy lung, reflecting the enlargement of distal airspaces caused by the tissue destruction that occurs in emphysema. Regional changes of the lung microstructure that occur in pulmonary diseases such as emphysema can thus be characterized by measuring the ADC of hyperpolarized gas in the lung (63–67).

Diffusion imaging of hyperpolarized ^{3}He in the lung has been investigated in a large number of research studies which have demonstrated the exquisite sensitivity of this method to both disease-induced alternations (63–67) and normal physiological variations in the microstructure of the human lung. For example, it has been shown that ADC measurements may reveal sub-clinical smoking-related emphysematous changes before they become apparent on high-resolution CT (68), and that ADC measurements can detect the subtle gravity-dependent gradient in alveolar size (69–71), as well as age-related changes in alveolar size (72,73). Detailed analysis of the signal behavior as a function of the degree of diffusion sensitization provides additional information about lung structure and, in particular, model-based (65,74) and “q-space” (75,76) approaches permit underlying structural dimensions to be estimated. Results from both of these techniques provide values that are comparable to those from histological measurements. For example, in a study of six human lung specimens including two normal lungs, two lungs with mild emphysema and two lungs with severe emphysema, Yablonskiy et al (74) found a strong correlation (R^2 = 0.985) between histological measurements of the mean linear intercept (a parameter commonly measured for histological evaluation of lung samples) and estimates of the mean linear intercept from ^{3}He diffusion data (see Fig. 4, ref. (74)).

As also discussed for ventilation imaging, it is reasonable to question whether the significant disparities between the physical properties of ^{129}Xe and those for ^{3}He will result in a substantial difference between information derived from diffusion-weighted ^{129}Xe measurements and that derived from diffusion-weighted ^{3}He measurements. Given that the diffusion coefficient for ^{129}Xe in air is about six times less than that for ^{3}He in air (Table 1), it is obvious that the specific ADC values measured with the two gases will be different. Nonetheless, the issue of importance is whether the relative changes in ADC values (or in other derived metrics) in response to pathological or physiological processes will differ substantially between ^{129}Xe and ^{3}He. Analogous to the situation for ventilation imaging, preliminary results from a small number of subjects suggest that diffusion imaging using ^{129}Xe indeed yields similar information to that from diffusion imaging using ^{3}He

(36,77). For example, the two methods are compared in Fig. 7, which shows ADC maps obtained in healthy subjects and subjects having COPD with emphysema. While the ADC values derived from both gases are relatively low and spatially uniform in the healthy subjects, both subjects with COPD demonstrate markedly inhomogeneous and generally elevated ADC values compared to the healthy subjects. As noted above, the elevation in ADC values for the subjects having COPD with emphysema reflects enlargement of the distal airspaces due to the disease process.

Previous studies using ^{3}He have shown that diffusion imaging using a relatively long sensitization time (~1 s, compared to ~1 ms in commonly used gradient-echo-based approaches) may provide improved sensitivity to certain microstructural changes associated with disease (78,79). Preliminary results indicate that these *long time scale* methods are also feasible using ^{129}Xe and yield results similar to those obtained using ^{3}He (50).

In a recent study including 8 COPD subjects with emphysema and 10 age-matched healthy controls, Kaushik et al found that the mean ADC value of ^{129}Xe for the COPD subjects was significantly elevated compared to that for the age-matched healthy controls (36). This study also demonstrated that ADC measurements using ^{129}Xe can detect the subtle gravity-dependent gradient in alveolar size (Fig. 8) and age-related increase in ADC values. In all, the ^{129}Xe diffusion results from Kaushik et al (36), as well as those from others (50,77), parallel earlier, analogous observations made using ^{3}He, supporting that diffusion imaging using ^{129}Xe and ^{3}He provide comparable information on the microstructure of the lung.

Partial-pressure of Oxygen

Pure hyperpolarized gases have relaxation times that are much longer than those for biological tissues. For example, in a properly-prepared glass container, the longitudinal (T1) relaxation time for pure ^{3}He can be tens of hours. When mixed with respiratory gases in the lung, interaction with paramagnetic oxygen substantially accelerates longitudinal relaxation of hyperpolarized gases, leading to a T1 value of roughly 20 s in the healthy human lung. Further, the longitudinal-relaxation rate (1/T1) in the lung is directly proportional to the concentration of oxygen (80). Thus, by acquiring image data from which maps of the T1 value can be calculated, the regional partial pressure of oxygen (pO_2) in the alveolar airspaces can be estimated (81). It is also possible to calculate regional ventilation-to-perfusion ratios from the partial-pressure data (82).

Although measurements of oxygen concentration have obvious practical applications for the study of the healthy and diseased lung, they are challenging to perform because the signal loss from T1 relaxation has the same functional form and a similar magnitude to that resulting from the application of the RF pulses required to collect the image data. This situation has led to substantial technical development aimed at optimizing the sensitivity and reproducibility of approaches for measuring alveolar pO_2 (83–87). Although previous research has been based largely on hyperpolarized ^{3}He, the primary considerations for performing oxygen-concentration measurements using ^{129}Xe are the same as those for ^{3}He. Thus, analogous to the situation for both ventilation and diffusion imaging, early studies in humans suggest that pO_2 measurements are not only feasible using ^{129}Xe (Fig. 9) (25,51), but also yield comparable information to those performed using ^{3}He. However, in contrast to the situation for ^{3}He, gas exchange and uptake in the lung play an important role for ^{129}Xe (as discussed below), accelerating the decay of the hyperpolarized magnetization. As a result, the *apparent* pO_2 measured using ^{129}Xe is biased upward (25,51), unless a correction for the effects of gas exchange and uptake is applied (25). Nonetheless, this bias is relatively modest at clinical field strengths (51).

Other Methods

A number of other techniques for characterizing the function and structure of the lung, such as dynamic imaging of gas flow or of magnetization tags during inhalation and exhalation, have been developed based on hyperpolarized ^{3}He. Although little experience exists with ^{129}Xe implementations of these methods, the results described above for ventilation, diffusion, and oxygen-concentration imaging suggest that, in general, the various methods developed using ^{3}He should successfully translate to ^{129}Xe.

GAS EXCHANGE AND UPTAKE

Upon inhalation, ^{129}Xe not only fills the airspaces of the lung, but also dissolves in the lung parenchyma and blood (Fig. 10). As a result, an MR spectrum obtained from the lung shows multiple peaks (12,18,19,88) associated with distinct physical compartments (Fig. 10, right). While most ^{129}Xe resides in the airspaces of the lung (so-called *gas-phase* xenon), and corresponds to a single large peak, approximately 2% is dissolved in the lung parenchyma and blood (so-called *dissolved-phase* xenon), and gives rise to two or more smaller peaks with chemical shifts of about 200 parts per million (ppm) from the gas peak (12,18,19,88). Note that the chemical-shift difference between gas-phase and dissolved-phase ^{129}Xe in the lung is about 60 times larger than the chemical-shift difference between protons in water and those in fat (~3.5 ppm). Driven by diffusion, ^{129}Xe atoms in the gas phase exchange continually with those in the dissolved compartments, and thus the small pool of dissolved-phase xenon exists in dynamic equilibrium with xenon in the airspaces (Fig. 11). This xenon exchange between the airspaces and parenchyma/blood, combined with the very large chemical shift difference between gas- and dissolved-phase ^{129}Xe (which corresponds to a frequency difference of ~3.5 kHz at 1.5T), form the basis for several imaging approaches for characterizing gas uptake and exchange in the lung. In this section we will describe two classes of such imaging methods -- *indirect* and *direct* measurements. Spectroscopic acquisitions of dissolved-phase ^{129}Xe in the human lung have also produced interesting results for characterizing gas uptake, exchange and transport; although these will not be discussed further, the interested reader is referred to references (25,26,89) for additional information.

Indirect Measurement

Although exchange and uptake of xenon offer interesting possibilities for producing images of relevance to lung function and disease, the signal available from dissolved-phase ^{129}Xe is limited by the small fraction of ^{129}Xe in the lung that dissolves in tissue or blood, making it challenging to produce images with high spatial resolution that directly depict the dissolved-phase compartments. To overcome this limitation, the xenon polarization transfer contrast technique (abbreviated XTC) takes advantage of the rapid, diffusion-driven exchange of xenon between the airspaces and dissolved-phase compartments (Fig. 11) to encode information on gas-exchange characteristics into gas-phase ^{129}Xe images of the lung (20,90). Since most inhaled ^{129}Xe resides in the airspaces, the relatively high gas-phase signal permits increased spatial resolution compared to that achievable through direct imaging of dissolved-phase ^{129}Xe.

The primary concepts underlying the XTC technique are illustrated in Fig. 12. First, following inhalation of hyperpolarized gas, an image of gas-phase ^{129}Xe (i.e., a ventilation image) is acquired using a low-flip-angle gradient-echo pulse sequence (Fig. 12, left). Next, a high-flip-angle (e.g., 90°) RF pulse is applied at the frequency corresponding to the dissolved-phase compartments (approximately +200 ppm from the gas-phase frequency), thereby substantially reducing or eliminating the dissolved-phase longitudinal magnetization (Fig. 12, plots in center). Immediately following this high-flip-angle RF pulse, ^{129}Xe atoms

in the tissue and blood diffuse into the airspaces, as ^{129}Xe atoms in the airspaces diffuse into the tissue and blood (Fig. 11). Since, immediately following the high-flip-angle RF pulse, the dissolved-phase longitudinal magnetization is depleted while the gas-phase magnetization, unaffected by the RF pulse, is relatively high, exchange of xenon atoms between the airspaces and tissue/blood causes the longitudinal magnetization of the dissolved-phase compartments to increase (Fig. 12, plot on right, gold and red curves) while that for the gas-phase decreases (Fig. 12, plot on right, blue curve). Although the decrease in the gas-phase longitudinal magnetization due to a single high-flip-angle RF pulse applied at the dissolved-phase frequency is relatively small, the effect can be amplified by applying a series of high-flip-angle RF pulses, with a delay time between RF pulses to permit exchange between the airspaces and tissue/blood (Fig. 12, plot on right). This scheme generates image contrast based on the characteristics of gas exchange since the gas-phase signal will decrease rapidly in regions with substantial exchange, but much more slowly in regions with little exchange. (For example, the signal decrease in healthy lung parenchyma is much larger than that in the large airways (20).) Following this series of *contrast-generating* high-flip-angle RF pulses, a second image of gas-phase ^{129}Xe is acquired (Fig. 12, right). Analysis of the changes in signal intensity between the first and second images provides a regional map (Fig. 12, top) reflecting the degree of gas exchange that occurred during the delay between contrast-generating RF pulses. For a relatively long delay between RF pulses, this map primarily reflects tissue density, while for a short delay between RF pulses, the map reflects alveolar surface-to-volume ratio (20,90).

During application of the contrast-generating RF pulses, the gas-phase ^{129}Xe magnetization also decreases due to T1 relaxation, xenon removal by blood flow, and any incidental effect of the contrast-generating RF pulses on gas-phase ^{129}Xe. These effects can be corrected in the XTC map by using information from a “control” acquisition, wherein the high-flip-angle RF pulses are applied at approximately −200 ppm (instead of +200 ppm) relative to the gas-phase resonance frequency (20). Nonetheless, for an appropriately designed XTC acquisition, the signal decrease due to the contrast-generating RF pulses is much larger than that due to T1 relaxation.

While the XTC technique was originally developed based on studies in animals (20,90), using separate breath-hold periods for the XTC and control acquisitions, Patz et al (25,26) first demonstrated a single breath-hold version of the method suitable for application in humans. An example of results from single breath-hold XTC measurements, performed at 0.2T, is shown in Fig. 13 (25). Maps of fractional gas exchange were obtained in a healthy subject at lung volumes corresponding to 47% and 63% of total lung capacity (TLC). The fractional gas exchange appeared fairly uniform across the lung in both cases, as expected in a healthy subject, while the mean value decreased by 22%, from 1.8% (47% of TLC) to 1.4% (63% of TLC), in response to the increase in lung volume and corresponding decrease in tissue density. Further, for 47% of TLC, summation of the values along the left-right direction revealed an increase in fractional gas exchange of roughly 0.5% from apex to base, whereas the corresponding values for 63% of TLC were uniform from apex to base (25). We see that XTC-based measurement of gas-exchange characteristics is sufficiently sensitive to detect the physiologic effects of a relatively small change in lung volume.

By making measurements at multiple values of the delay between contrast-generating RF pulses (so-called multiple-exchange-time XTC, or MXTC), and using a simple model for the process of gas exchange between airspaces and tissue/blood, the values of certain parameters describing lung microstructure can be estimated using the XTC technique. This approach was recently demonstrated by Dregely et al (91), who derived the parameters “MXTC-F,” which is proportional to the tissue to alveolar-volume ratio (essentially, tissue density), and “MXTC-S,” which is proportional to the mean septal wall thickness (i.e., the thickness of

the barrier, composed of tissue and blood, separating alveoli; see Fig. 11). Figure 14 shows maps of MXTC-F and MXTC-S derived from 3D acquisitions in a healthy volunteer (Fig. 14, upper row) and in a subject with moderate COPD (Fig. 14, lower row). For the healthy volunteer, the parameter MXTC-F was generally uniform within each coronal section, but clearly increased toward the posterior of the lung. This increase is consistent with the well-known gravity-induced gradient in lung tissue density from anterior to posterior in the supine position. In contrast, MXTC-F for the COPD subject showed substantial regional variation within each coronal section, with markedly lower values in the apices. A CT scan performed in this subject (Fig. 4, ref. (91)) indicated that regions of low MXTC-F values in the apices correspond to tissue loss, presumably due to emphysema. Similar to the behavior for MXTC-F, the parameter MXTC-S demonstrated relatively small variations within each coronal section for the healthy volunteer, while also clearly increasing toward the posterior of the lung. In contrast, MXTC-S values for the COPD subject did not show substantial variation along the anterior-posterior direction, but were generally higher than those in the healthy subject. This latter finding suggests that septal walls were thickened in the COPD subject, even in emphysematous regions that show tissue loss but presumably maintain residual alveolar structure. These preliminary results suggest that characterizing the lung using parameters derived from XTC measurements may offer interesting new possibilities for assessing lung disease.

Direct Measurement

Although interesting information regarding gas exchange in the lung, including the consequences of pathological alterations, can be obtained using indirect measurements such as performed with the XTC method discussed above, direct depiction of the dissolved compartments offers a different and physiologically-relevant perspective on gas uptake in the lung. Direct detection of dissolved-phase ^{129}Xe was demonstrated in early studies of the human lung, but the associated SNRs were too low for acquisition of dissolved-phase images (12). Images of the dissolved phase were later acquired in animals using multiple inhalations of hyperpolarized ^{129}Xe (23,92,93), although a multiple-inhalation approach is not feasible in humans using current technology. Nonetheless, recent improvements in gas-polarization technology (28) permit liter quantities of hyperpolarized ^{129}Xe to be obtained with sufficiently high polarization to make direct dissolved-phase imaging in humans feasible during a single breath-hold period. In 2010, two research groups (Cleveland et al (94) and Mugler et al (95)) published results showing direct imaging of dissolved-phase ^{129}Xe in the human lung.

An important consideration in the design of pulse sequences for direct imaging of dissolved-phase xenon is that ^{129}Xe in the airspaces acts as a reservoir for the dissolved-phase compartments. Thus, relatively high-flip angles can be applied to ^{129}Xe in the dissolved-phase compartments, which helps to compensate for the small fraction of xenon in the lung that is dissolved (94,95), because following a high-flip-angle RF pulse gas exchange replenishes the dissolved-phase compartments with a time constant on the order of 10 ms. Considering the large frequency difference between gas-phase and dissolved-phase ^{129}Xe, it is straightforward to implement RF pulses that result in a high flip-angle at the dissolved-phase frequency, but either a negligible (94) or relatively low (95) flip angle at the gas-phase frequency (e.g., see Fig. 1B in ref. (95)). Further, this large frequency difference can be used to acquire images that depict both the gas-phase and dissolved-phase components of ^{129}Xe, side-by-side, along the readout direction (95). Simultaneous acquisition of both components, with matched spatial resolution, permits regional quantification of gas uptake by normalizing the dissolved-phase signals by the gas-phase signals.

An example of direct dissolved-phase imaging is shown in Fig. 15 (95). For each section from the 3D acquisitions (Fig. 15a), gas-phase ^{129}Xe (reflecting ventilation) is on the left

and dissolved-phase ^{129}Xe (reflecting gas uptake) is on the right. The healthy subject (Fig. 15a, top) showed generally uniform distributions of gas-phase and dissolved-phase signal intensities throughout the lung, as expected, although the dissolved-phase signal intensity in the posterior portion of the lung was noticeably higher than that in the anterior portion, consistent with a gravity-induced gradient in lung tissue density from anterior to posterior in the supine position as described above for XTC results. In contrast, for the subject with mild COPD, both gas-phase and dissolved-phase components showed non-uniform signal distributions (Fig. 15a, bottom). Even though the distribution of ^{129}Xe in the airspaces modulates the amount of xenon available for exchange, signal intensity variations in the dissolved-phase components were not identical to those in the corresponding gas-phase components. Further, the signal intensity of the dissolved-phase component in the anterior portion of the lung of the COPD subject (Fig. 15a, bottom, first two images) was clearly higher than that for the corresponding gas-phase component, whereas the signal intensities for gas-phase and dissolved-phase components were similar in the anterior portion of the lung for the healthy subject. This difference between the healthy and COPD subjects is illustrated clearly by calculating the ratio of the dissolved-phase to gas-phase signals (Fig. 15b, top two rows); in the anterior sections of the lung, this ratio is substantially higher in the subject with mild COPD than in the healthy subject, which may reflect inflammation in the subject with mild COPD. There are several regions in the ratio images for the COPD subject (Fig. 15b, middle row) for which values are relatively low, and similar to those in the healthy subject. However, comparison of the ratio images to ADC maps (Fig. 15b, lower row) acquired in the COPD subject (albeit at slightly different section positions) reveals a high degree of correspondence between reduced ratio values and elevated ADC values (e.g., arrowheads), which indicate regions of dilated airspaces, presumably due to emphysematous changes.

The preliminary results from methods for direct imaging of ^{129}Xe dissolved in the human lung (94,95) suggest that these approaches will provide new opportunities for quantifying relationships among gas delivery, exchange, and transport, and thus show substantial potential to broaden our understanding of lung disease. Although initial results for direct imaging provided relatively coarse spatial resolution and only moderate SNR, it is reasonable to anticipate that technical advances can provide marked improvements.

FUTURE AS A CLINICAL TOOL

Unfortunately, since the sale of just a few gas-polarization systems by a company (MITI, Durham, NC; see Fig. 1) in the mid-1990s, it has not been possible to purchase a commercial polarizer in the US due to the business policies of the companies that have held exclusive rights to very broad patents in the hyperpolarized-gas field. Researchers in hyperpolarized-gas MRI have had polarizers on loan from the controlling companies, or have custom-built their own. This situation is the primary reason that, to date, hyperpolarized-gas MRI has failed to disseminate beyond a small handful of primarily academic centers. However, two *game-changing* developments occurred in the latter part of 2011. First, the company holding exclusive rights to the very broad patents in recent years offered to sell gas-polarization systems to the institutions that had them on loan. Many, if not all, of these institutions took advantage of the offer, which now makes it possible for these institutions to pursue research directions that were off limits when the polarization systems were under company control. The second, and more important, development is that a new company (Polarean, Inc., Research Triangle Park, NC) has formed which now has control of the intellectual-property portfolio that includes the very broad patents in the field of hyperpolarized-gas imaging. This company is dedicated to the development of hyperpolarized-gas MRI, in contrast to previous controlling companies, and, for the first time since the mid-1990s, offers gas-polarization systems for sale. This provides a clear path

for new centers to become involved in hyperpolarized-gas MRI, which is critical for development of the field.

This article has reviewed a number of the unique strategies for evaluating the structure and function of the human lung provided by MRI using hyperpolarized ^{129}Xe, including methods for assessing gas uptake and exchange which are beyond the capabilities of hyperpolarized ^{3}He. Now that recent changes in the commercial landscape of the field make it possible for this innovative technology to spread beyond a few centers, we will hopefully see, in the next several years, whether these interesting methods can move beyond research labs to become methods of choice for the routine evaluation and monitoring of pulmonary disease.

Acknowledgments

The authors thank Drs. James R. Brookeman, G. Wilson Miller and Kai Ruppert for helpful discussions.

Grant support: Supported in part by Siemens Medical Solutions and by NIH grants R01 HL109618, R01 HL079077, and R42 HL082013 from the National Heart, Lung, and Blood Institute. The content is solely the responsibility of the authors and does not necessarily represent the official views of the National Heart, Lung, and Blood Institute or the National Institutes of Health.

REFERENCES

1. Hatabu H, Alsop DC, Listerud J, Bonnet M, Gefter WB. T2* and proton density measurement of normal human lung parenchyma using submillisecond echo time gradient echo magnetic resonance imaging. Eur J Radiol. 1999; 29(3):245–252. [PubMed: 10399610]
2. Stock KW, Chen Q, Hatabu H, Edelman RR. Magnetic resonance T2* measurements of the normal human lung in vivo with ultra-short echo times. Magn Reson Imaging. 1999; 17(7):997–1000. [PubMed: 10463650]
3. Ohno Y, Koyama H, Yoshikawa T, et al. T2* measurements of 3-T MRI with ultrashort TEs: capabilities of pulmonary function assessment and clinical stage classification in smokers. AJR Am J Roentgenol. 2011; 197:W279–W285. [PubMed: 21785054]
4. Salerno M, Altes TA, Mugler JP 3rd, Nakatsu M, Hatabu H, de Lange EE. Hyperpolarized noble gas MR imaging of the lung: potential clinical applications. Eur J Radiol. 2001; 40(1):33–44. [PubMed: 11673006]
5. Möller HE, Chen XJ, Saam B, et al. MRI of the lungs using hyperpolarized noble gases. Magn Reson Med. 2002; 47(6):1029–1051. [PubMed: 12111949]
6. van Beek EJ, Wild JM, Kauczor HU, Schreiber W, Mugler JP 3rd, de Lange EE. Functional MRI of the lung using hyperpolarized 3-helium gas. J Magn Reson Imaging. 2004; 20(4):540–554. [PubMed: 15390146]
7. Matsuoka S, Patz S, Albert MS, et al. Hyperpolarized gas MR imaging of the lung: current status as a research tool. J Thorac Imaging. 2009; 24(3):181–188. [PubMed: 19704321]
8. Fain S, Schiebler ML, McCormack DG, Parraga G. Imaging of lung function using hyperpolarized helium-3 magnetic resonance imaging: review of current and emerging translational methods and applications. J Magn Reson Imaging. 2010; 32(6):1398–1408. [PubMed: 21105144]
9. Happer W, Miron E, Schaefer S, Schreiber D, van Wijngaarden WA, Zeng X. Polarization of the nuclear spins of noble-gas atoms by spin exchange with optically pumped alkali-metal atoms. Phys Rev A. 1984; 29(6):3092–3110.
10. Driehuys B, Cates GD, Miron E, Sauer K, Walter DK, Happer W. High-volume production of laser-polarized ^{129}Xe. Appl Phys Lett. 1996; 69(12):1668–1670.
11. Albert MS, Cates GD, Driehuys B, et al. Biological magnetic resonance imaging using laser-polarized ^{129}Xe. Nature. 1994; 370(6486):199–201. [PubMed: 8028666]
12. Mugler JP 3rd, Driehuys B, Brookeman JR, et al. MR imaging and spectroscopy using hyperpolarized ^{129}Xe gas: preliminary human results. Magn Reson Med. 1997; 37(6):809–815. [PubMed: 9178229]

13. Feder, T. US government agencies work to minimize damage due to helium-3 shortfall; Physics Today. 2009 Oct. p. 21-23.
14. Cho A. Helium-3 shortage could put freeze on low-temperature research. Science. 2009 Nov 6.326:778–779. [PubMed: 19892947]
15. Kramer D. DOE begins rationing helium-3. Physics Today. 2010 Jun.:22–25.
16. Abraham MH, Kamlet MJ, Taft RW, Doherty RM, Weathersby PK. Solubility properties in polymers and biological media. 2. The correlation and prediction of the solubilities of nonelectrolytes in biological tissues and fluids. J Med Chem. 1985; 28(7):865–870. [PubMed: 4009609]
17. Miller KW, Reo NV, Schoot Uiterkamp AJ, Stengle DP, Stengle TR, Williamson KL. Xenon NMR: chemical shifts of a general anesthetic in common solvents, proteins, and membranes. Proc Natl Acad Sci USA. 1981; 78(8):4946–4949. [PubMed: 6946442]
18. Sakai K, Bilek AM, Oteiza E, et al. Temporal dynamics of hyperpolarized ^{129}Xe resonances in living rats. J Magn Reson B. 1996; 111(3):300–304. [PubMed: 8661297]
19. Ruppert K, Brookeman JR, Hagspiel KD, Driehuys B, Mugler JP 3rd. NMR of hyperpolarized ^{129}Xe in the canine chest: spectral dynamics during a breath-hold. NMR Biomed. 2000; 13(4): 220–228. [PubMed: 10867700]
20. Ruppert K, Brookeman JR, Hagspiel KD, Mugler JP 3rd. Probing lung physiology with xenon polarization transfer contrast (XTC). Magn Reson Med. 2000; 44(3):349–357. [PubMed: 10975884]
21. Butler JP, Mair RW, Hoffmann D, et al. Measuring surface-area-to-volume ratios in soft porous materials using laser-polarized xenon interphase exchange nuclear magnetic resonance. J Phys Condens Matter. 2002; 14(13):L297–L304. [PubMed: 12741395]
22. Mansson S, Wolber J, Driehuys B, Wollmer P, Golman K. Characterization of diffusing capacity and perfusion of the rat lung in a lipopolysaccaride disease model using hyperpolarized ^{129}Xe. Magn Reson Med. 2003; 50(6):1170–1179. [PubMed: 14648564]
23. Driehuys B, Cofer GP, Pollaro J, Mackel JB, Hedlund LW, Johnson GA. Imaging alveolar-capillary gas transfer using hyperpolarized ^{129}Xe MRI. Proc Natl Acad Sci USA. 2006; 103(48): 18278–18283. [PubMed: 17101964]
24. Abdeen N, Cross A, Cron G, et al. Measurement of xenon diffusing capacity in the rat lung by hyperpolarized ^{129}Xe MRI and dynamic spectroscopy in a single breath-hold. Magn Reson Med. 2006; 56(2):255–264. [PubMed: 16767751]
25. Patz S, Hersman FW, Muradian I, et al. Hyperpolarized ^{129}Xe MRI: a viable functional lung imaging modality? Eur J Radiol. 2007; 64(3):335–344. [PubMed: 17890035]
26. Patz S, Muradian I, Hrovat MI, et al. Human pulmonary imaging and spectroscopy with hyperpolarized ^{129}Xe at 0.2T. Acad Radiol. 2008; 15(6):713–727. [PubMed: 18486008]
27. Driehuys B, Möller HE, Cleveland ZI, Pollaro J, Hedlund LW. Pulmonary perfusion and xenon gas exchange in rats: MR imaging with intravenous injection of hyperpolarized ^{129}Xe. Radiology. 2009; 252(2):386–393. [PubMed: 19703880]
28. Hersman FW, Ruset IC, Ketel S, et al. Large production system for hyperpolarized ^{129}Xe for human lung imaging studies. Acad Radiol. 2008; 15(6):683–692. [PubMed: 18486005]
29. Middleton H, Black RD, Saam B, et al. MR imaging with hyperpolarized ^{3}He gas. Magn Reson Med. 1995; 33(2):271–275. [PubMed: 7707920]
30. Black RD, Middleton HL, Cates GD, et al. In vivo He-3 MR images of guinea pig lungs. Radiology. 1996; 199(3):867–870. [PubMed: 8638019]
31. Edelstein WA, Glover GH, Hardy CJ, Redington RW. The intrinsic signal-to-noise ratio in NMR imaging. Magn Reson Med. 1986; 3(4):604–618. [PubMed: 3747821]
32. Lee RF, Johnson G, Grossman RI, Stoeckel B, Trampel R, McGuinness G. Advantages of parallel imaging in conjunction with hyperpolarized helium--a new approach to MRI of the lung. Magn Reson Med. 2006; 55(5):1132–1141. [PubMed: 16586457]
33. Dregely, IM.; Wiggins, GC.; Ruset, IC., et al. A 32 channel phased array lung coil for parallel imaging with hyperpolarized xenon 129 at 3T (abstract). Proceedings of the 17th Annual Meeting of ISMRM; Honolulu, Hawaii, USA. 2009. p. 2203

34. Meise FM, Rivoire J, Terekhov M, et al. Design and evaluation of a 32-channel phased-array coil for lung imaging with hyperpolarized 3-helium. Magn Reson Med. 2010; 63(2):456–464. [PubMed: 20099333]
35. Deppe MH, Parra-Robles J, Marshall H, Lanz T, Wild JM. A flexible 32-channel receive array combined with a homogeneous transmit coil for human lung imaging with hyperpolarized ^{3}He at 1.5 T. Magn Reson Med. 2011
36. Kaushik SS, Cleveland ZI, Cofer GP, et al. Diffusion-weighted hyperpolarized ^{129}Xe MRI in healthy volunteers and subjects with chronic obstructive pulmonary disease. Magn Reson Med. 2011; 65(4):1154–1165. [PubMed: 21413080]
37. Driehuys B, Martinez-Jimenez S, Cleveland ZI, et al. Chronic obstructive pulmonary disease: safety and tolerability of hyperpolarized ^{129}Xe MR imaging in healthy volunteers and patients. Radiology. 2012; 262(1):279–289. [PubMed: 22056683]
38. Bouchiat MA, Carver TR, Varnum CM. Nuclear polarization in ^{3}He gas induced by optical pumping and dipolar exchange. Phys Rev Lett. 1960; 5:373–375.
39. Ruset IC, Ketel S, Hersman FW. Optical pumping system design for large production of hyperpolarized ^{129}Xe. Phys Rev Lett. 2006; 96(5) 053002.
40. Gierada DS, Saam B, Yablonskiy D, Cooper JD, Lefrak SS, Conradi MS. Dynamic echo planar MR imaging of lung ventilation with hyperpolarized ^{3}He in normal subjects and patients with severe emphysema. NMR Biomed. 2000; 13(4):176–181. [PubMed: 10867693]
41. Durand E, Guillot G, Darrasse L, et al. CPMG measurements and ultrafast imaging in human lungs with hyperpolarized helium-3 at low field (0.1 T). Magn Reson Med. 2002; 47(1):75–81. [PubMed: 11754445]
42. Mugler, JP, 3rd. Optimization of gradient-echo sequences for hyperpolarized noble gas MRI (abstract). Proceedings of the 6th Annual Meeting of ISMRM; Sydney, Australia. 1998. p. 1904
43. Mugler, JR., 3rd; Brookeman, JR. Signal-to-noise considerations for parallel imaging with hyperpolarized gases (abstract). Proceedings of the 13th Annual Meeting of ISMRM; Miami. 2005. p. 485
44. Zhao L, Venkatesh AK, Albert MS, Panych LP. Signal-to-noise ratio comparison of encoding methods for hyperpolarized noble gas MRI. J Magn Reson. 2001; 148(2):314–326. [PubMed: 11237637]
45. Wild JM, Paley MN, Viallon M, Schreiber WG, van Beek EJ, Griffiths PD. k-space filtering in 2D gradient-echo breath-hold hyperpolarized ^{3}He MRI: spatial resolution and signal-to-noise ratio considerations. Magn Reson Med. 2002; 47(4):687–695. [PubMed: 11948729]
46. Miller GW, Altes TA, Brookeman JR, De Lange EE, Mugler JP 3rd. Hyperpolarized ^{3}He lung ventilation imaging with B1-inhomogeneity correction in a single breath-hold scan. Magma. 2004; 16(5):218–226. [PubMed: 15108030]
47. Wild JM, Woodhouse N, Paley MN, et al. Comparison between 2D and 3D gradient-echo sequences for MRI of human lung ventilation with hyperpolarized ^{3}He. Magn Reson Med. 2004; 52(3):673–678. [PubMed: 15334590]
48. Altes, TA.; Mugler, JP.; Dregely, IM., et al. Hyperpolarized xenon-129 ventilation MRI: preliminary results in normal subjects and patients with lung disease (abstract). Proceedings of the 18th Annual Meeting of ISMRM; Stockholm. 2010. p. 2529
49. Driehuys, B.; Cleveland, ZI.; Nouls, J., et al. Quantitative scoring of hyperpolarized ^{129}Xe ventilation imaging: correlation with pulmonary function testing and age (abstract). Proceedings of the 19th Annual Meeting of ISMRM; Montreal. 2011. p. 550
50. Wang, C.; Mugler, JP., 3rd; de Lange, EE., et al. Measurement of the diffusion of hyperpolarized ^{129}Xe in human lungs over short and long time scales during one breath hold (abstract). Proceedings of the 18th Annual Meeting of ISMRM; Stockholm. 2010. p. 2543
51. Miller, GW.; Mugler, JP., 3rd; Altes, TA., et al. Motion-corrected pO_2 mapping in human lungs using hyperpolarized Xe-129 MRI (abstract). Proceedings of the 18th Annual Meeting of ISMRM; Stockholm. 2010. p. 2558
52. MacFall JR, Charles HC, Black RD, et al. Human lung air spaces: potential for MR imaging with hyperpolarized He-3. Radiology. 1996; 200(2):553–558. [PubMed: 8685356]

53. Kauczor HU, Hofmann D, Kreitner KF, et al. Normal and abnormal pulmonary ventilation: visualization at hyperpolarized He-3 MR imaging. Radiology. 1996; 201(2):564–568. [PubMed: 8888259]
54. Kauczor HU, Ebert M, Kreitner KF, et al. Imaging of the lungs using ^{3}He MRI: preliminary clinical experience in 18 patients with and without lung disease. J Magn Reson Imaging. 1997; 7(3):538–543. [PubMed: 9170039]
55. Donnelly LF, MacFall JR, McAdams HP, et al. Cystic fibrosis: combined hyperpolarized ^{3}He-enhanced and conventional proton MR imaging in the lung--preliminary observations. Radiology. 1999; 212(3):885–889. [PubMed: 10478261]
56. Altes TA, Powers PL, Knight-Scott J, et al. Hyperpolarized ^{3}He MR lung ventilation imaging in asthmatics: preliminary findings. J Magn Reson Imaging. 2001; 13(3):378–384. [PubMed: 11241810]
57. Deninger AJ, Mansson S, Petersson JS, et al. Quantitative measurement of regional lung ventilation using ^{3}He MRI. Magn Reson Med. 2002; 48(2):223–232. [PubMed: 12210930]
58. Santyr GE, Lam WW, Ouriadov A. Rapid and efficient mapping of regional ventilation in the rat lung using hyperpolarized ^{3}He with Flip Angle Variation for Offset of RF and Relaxation (FAVOR). Magn Reson Med. 2008; 59(6):1304–1310. [PubMed: 18506796]
59. Emami K, Kadlecek SJ, Woodburn JM, et al. Improved technique for measurement of regional fractional ventilation by hyperpolarized ^{3}He MRI. Magn Reson Med. 2010; 63(1):137–150. [PubMed: 19877277]
60. Cai J, Altes TA, Miller GW, et al. MR grid-tagging using hyperpolarized helium-3 for regional quantitative assessment of pulmonary biomechanics and ventilation. Magn Reson Med. 2007; 58(2):373–380. [PubMed: 17654579]
61. Deppe MH, Parra-Robles J, Ajraoui S, Wild JM. Combined measurement of pulmonary inert gas washout and regional ventilation heterogeneity by MR of a single dose of hyperpolarized ^{3}He. Magn Reson Med. 2011; 65(4):1075–1083. [PubMed: 21413071]
62. Kabilan S, Lin CL, Hoffman EA. Characteristics of airflow in a CT-based ovine lung: a numerical study. J Appl Physiol. 2007; 102(4):1469–1482. [PubMed: 17110504]
63. Saam BT, Yablonskiy DA, Kodibagkar VD, et al. MR imaging of diffusion of ^{3}He gas in healthy and diseased lungs. Magn Reson Med. 2000; 44(2):174–179. [PubMed: 10918314]
64. Salerno M, de Lange EE, Altes TA, Truwit JD, Brookeman JR, Mugler JP 3rd. Emphysema: hyperpolarized helium 3 diffusion MR imaging of the lungs compared with spirometric indexes--initial experience. Radiology. 2002; 222(1):252–260. [PubMed: 11756734]
65. Yablonskiy DA, Sukstanskii AL, Leawoods JC, et al. Quantitative in vivo assessment of lung microstructure at the alveolar level with hyperpolarized ^{3}He diffusion MRI. Proc Natl Acad Sci U S A. 2002; 99(5):3111–3116. [PubMed: 11867733]
66. Swift AJ, Wild JM, Fichele S, et al. Emphysematous changes and normal variation in smokers and COPD patients using diffusion ^{3}He MRI. Eur J Radiol. 2005; 54(3):352–358. [PubMed: 15899335]
67. Kirby M, Mathew L, Wheatley A, Santyr GE, McCormack DG, Parraga G. Chronic obstructive pulmonary disease: longitudinal hyperpolarized ^{3}He MR imaging. Radiology. 2010; 256(1):280–289. [PubMed: 20574101]
68. Fain SB, Panth SR, Evans MD, et al. Early emphysematous changes in asymptomatic smokers: detection with ^{3}He MR imaging. Radiology. 2006; 239(3):875–883. [PubMed: 16714465]
69. Salerno, M.; Brookeman, JR.; de Lange, EE.; Knight-Scott, J.; Mugler, JP, 3rd. Demonstration of an alveolar-size gradient in the healthy human lung: a study of the reproducibility of hyperpolarized ^{3}He diffusion MRI (abstract). Proceedings of the 8th Annual Meeting of ISMRM; Denver, CO, USA. 2000. p. 2195
70. Salerno M, Altes TA, Brookeman JR, de Lange EE, Mugler JP 3rd. Rapid hyperpolarized ^{3}He diffusion MRI of healthy and emphysematous human lungs using an optimized interleaved-spiral pulse sequence. J Magn Reson Imaging. 2003; 17(5):581–588. [PubMed: 12720268]
71. Fichele S, Woodhouse N, Swift AJ, et al. MRI of helium-3 gas in healthy lungs: posture related variations of alveolar size. J Magn Reson Imaging. 2004; 20(2):331–335. [PubMed: 15269962]

72. Fain SB, Altes TA, Panth SR, et al. Detection of age-dependent changes in healthy adult lungs with diffusion-weighted ^{3}He MRI. Acad Radiol. 2005; 12(11):1385–1393. [PubMed: 16253850]
73. Altes TA, Mata J, de Lange EE, Brookeman JR, Mugler JP 3rd. Assessment of lung development using hyperpolarized helium-3 diffusion MR imaging. J Magn Reson Imaging. 2006; 24(6):1277–1283. [PubMed: 17096396]
74. Yablonskiy DA, Sukstanskii AL, Woods JC, et al. Quantification of lung microstructure with hyperpolarized ^{3}He diffusion MRI. J Appl Physiol. 2009; 107:1258–1265. [PubMed: 19661452]
75. Shanbhag DD, Altes TA, Miller GW, Mata JF, Knight-Scott J. q-Space analysis of lung morphometry in vivo with hyperpolarized ^{3}He spectroscopy. J Magn Reson Imaging. 2006; 24(1): 84–94. [PubMed: 16767705]
76. O'Halloran RL, Holmes JH, Wu YC, Alexander A, Fain SB. Helium-3 MR q-space imaging with radial acquisition and iterative highly constrained back-projection. Magn Reson Med. 2010; 63(1): 41–50. [PubMed: 19953515]
77. Flors, L.; Mugler, J.; Ruppert, K.; Ruset, I.; Hersman, F.; Altes, T. Hyperpolarized xenon-129 diffusion MRI of the lungs: a viable alternative to helium-3 (abstract). 96th Scientific Assembly and Annual Meeting Program, Radiological Society of North America; Chicago, IL, USA. 2010. p. SSQ04-09
78. Woods JC, Yablonskiy DA, Chino K, Tanoli TS, Cooper JD, Conradi MS. Magnetization tagging decay to measure long-range ^{3}He diffusion in healthy and emphysematous canine lungs. Magn Reson Med. 2004; 51(5):1002–1008. [PubMed: 15122683]
79. Wang C, Miller GW, Altes TA, de Lange EE, Cates GD Jr, Mugler JP 3rd. Time dependence of ^{3}He diffusion in the human lung: measurement in the long-time regime using stimulated echoes. Magn Reson Med. 2006; 56(2):296–309. [PubMed: 16791861]
80. Saam B, Happer W, Middleton H. Nuclear relaxation of ^{3}He in the presence of O_2. Phys Rev A. 1995; 52(1):862–865. [PubMed: 9912313]
81. Deninger AJ, Eberle B, Ebert M, et al. Quantification of regional intrapulmonary oxygen partial pressure evolution during apnea by ^{3}He MRI. J Magn Reson. 1999; 141(2):207–216. [PubMed: 10579944]
82. Rizi RR, Baumgardner JE, Ishii M, et al. Determination of regional VA/Q by hyperpolarized ^{3}He MRI. Magn Reson Med. 2004; 52(1):65–72. [PubMed: 15236368]
83. Deninger AJ, Eberle B, Bermuth J, et al. Assessment of a single-acquisition imaging sequence for oxygen-sensitive ^{3}He-MRI. Magn Reson Med. 2002; 47(1):105–114. [PubMed: 11754449]
84. Fischer MC, Spector ZZ, Ishii M, et al. Single-acquisition sequence for the measurement of oxygen partial pressure by hyperpolarized gas MRI. Magn Reson Med. 2004; 52(4):766–773. [PubMed: 15389934]
85. Wild JM, Fichele S, Woodhouse N, Paley MN, Kasuboski L, van Beek EJ. 3D volume-localized pO_2 measurement in the human lung with ^{3}He MRI. Magn Reson Med. 2005; 53(5):1055–1064. [PubMed: 15844148]
86. Yu J, Ishii M, Law M, et al. Optimization of scan parameters in pulmonary partial pressure oxygen measurement by hyperpolarized ^{3}He MRI. Magn Reson Med. 2008; 59(1):124–131. [PubMed: 18050348]
87. Miller GW, Mugler JP 3rd, Altes TA, et al. A short-breath-hold technique for lung pO_2 mapping with ^{3}He MRI. Magn Reson Med. 2010; 63(1):127–136. [PubMed: 19918891]
88. Wagshul ME, Button TM, Li HF, et al. In vivo MR imaging and spectroscopy using hyperpolarized ^{129}Xe. Magn Reson Med. 1996; 36(2):183–191. [PubMed: 8843370]
89. Patz S, Muradyan I, Hrovat MI, et al. Diffusion of hyperpolarized ^{129}Xe in the lung: a simplified model of ^{129}Xe septal uptake and experimental results. New J Phys. 2011; 13 015009.
90. Ruppert K, Mata JF, Brookeman JR, Hagspiel KD, Mugler JP 3rd. Exploring lung function with hyperpolarized ^{129}Xe nuclear magnetic resonance. Magn Reson Med. 2004; 51(4):676–687. [PubMed: 15065239]
91. Dregely I, Mugler JP 3rd, Ruset IC, et al. Hyperpolarized xenon-129 gas-exchange imaging of lung microstructure: first case studies in subjects with obstructive lung disease. J Mag Reson Imaging. 2011; 33(5):1052–1062.

92. Swanson SD, Rosen MS, Coulter KP, Welsh RC, Chupp TE. Distribution and dynamics of laser-polarized ^{129}Xe magnetization in vivo. Magn Reson Med. 1999; 42(6):1137–1145. [PubMed: 10571936]

93. Wakayama T, Narazaki M, Kimura A, Fujiwara H. Hyperpolarized ^{129}Xe phase-selective imaging of mouse lung at 9.4T using a continuous-flow hyperpolarizing system. Magn Reson Med Sci. 2008; 7(2):65–72. [PubMed: 18603837]

94. Cleveland ZI, Cofer GP, Metz G, et al. Hyperpolarized ^{129}Xe MR imaging of alveolar gas uptake in humans. PLoS ONE. 2010; 5(8):e12192. [PubMed: 20808950]

95. Mugler JP 3rd, Altes TA, Ruset IC, et al. Simultaneous magnetic resonance imaging of ventilation distribution and gas uptake in the human lung using hyperpolarized xenon-129. Proc Natl Acad Sci U S A. 2010; 107(50):21707–21712. [PubMed: 21098267]

96. Bock M. Simultaneous T2* and diffusion measurements with ^{3}He. Magn Reson Med. 1997; 38(6): 890–895. [PubMed: 9402189]

97. Patyal BR, Gao JH, Williams RF, et al. Longitudinal relaxation and diffusion measurements using magnetic resonance signals from laser-hyperpolarized ^{129}Xe nuclei. J Magn Reson. 1997; 126(1): 58–65. [PubMed: 9177796]

98. Chen XJ, Moller HE, Chawla MS, et al. Spatially resolved measurements of hyperpolarized gas properties in the lung in vivo. Part I: diffusion coefficient. Magn Reson Med. 1999; 42(4):721–728. [PubMed: 10502761]

99. de Lange EE, Mugler JP 3rd, Brookeman JR, et al. Lung air spaces: MR imaging evaluation with hyperpolarized ^{3}He gas. Radiology. 1999; 210(3):851–857. [PubMed: 10207491]

100. Altes, TA.; Mugler, JP.; Meyer, C., et al. A comparison of hyperpolarized helium-3 and xenon-129 MR ventilation imaging in cystic fibrosis (abstract). Proceedings of the 20th Annual Meeting of ISMRM; Melbourne, Australia. 2012. p. 1354

101. Miller, GW.; Mugler, JP., 3rd; Altes, TA., et al. Cardiac triggering suppresses heart-motion artifacts in hyperpolarized-gas lung pO_2 maps (abstract). Proceedings of the 20th Annual Meeting of ISMRM; Melbourne, Australia. 2012. p. 1351

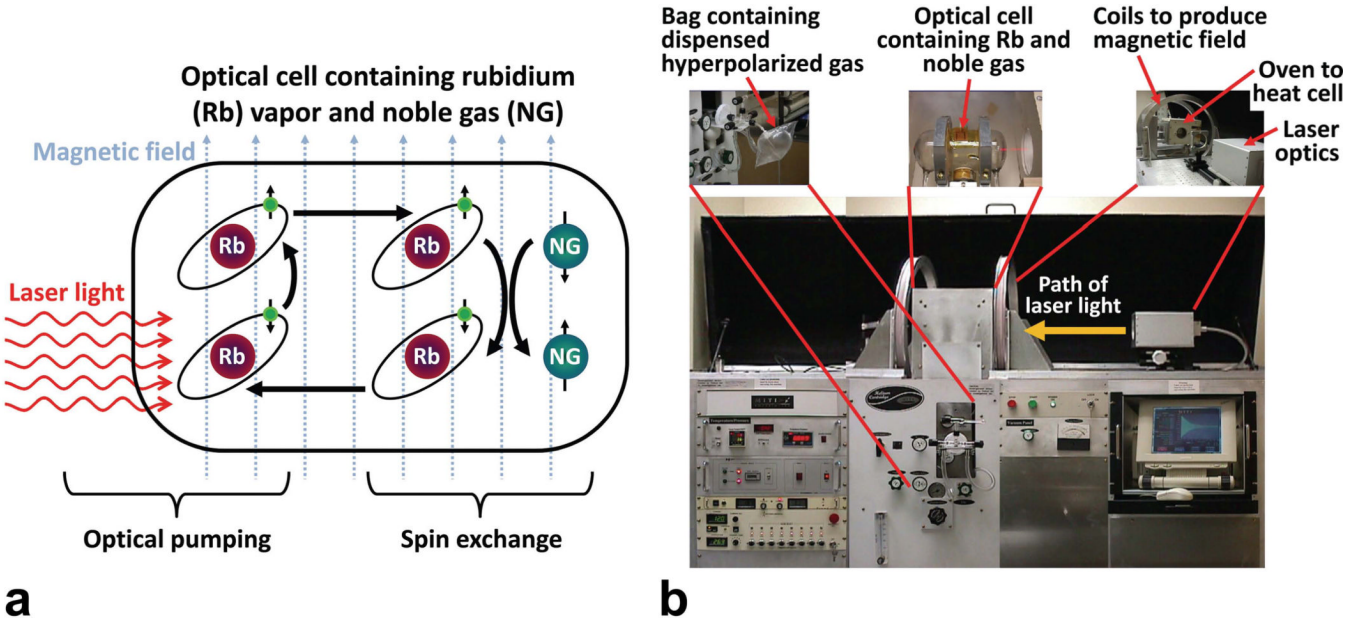

Figure 1.

Optical pumping and spin exchange. (**a**) Simplified conceptual diagram of the optical-pumping and spin-exchange process. In optical pumping (left), circularly-polarized laser light at the appropriate wavelength polarizes the spins of the valence electrons (shown in green) of rubidium atoms by preferentially populating one of the two spin states for the valence electron. In this diagram, electron-spin polarization is illustrated by a change in the electron-spin orientation (symbolized by the small black arrow through the electron) from down to up. Spin-exchange collisions (right) transfer this polarization from rubidium electrons to noble-gas nuclei. After spin exchange, the spins of the valence electrons of rubidium atoms are polarized again and participate in subsequent spin-exchange collisions, further increasing the noble-gas polarization. (Diagram adapted from Fig. 1 of ref. (99).) (**b**) Photograph of an early prototype commercial gas-polarization system (model IGI 9600, Magnetic Imaging Technologies, Inc. [MITI], Durham, NC), showing some of the system's major functional aspects. This system, the first manufactured by MITI, has an exchangeable central "cartridge" to permit operation with either ^{129}Xe or ^{3}He.

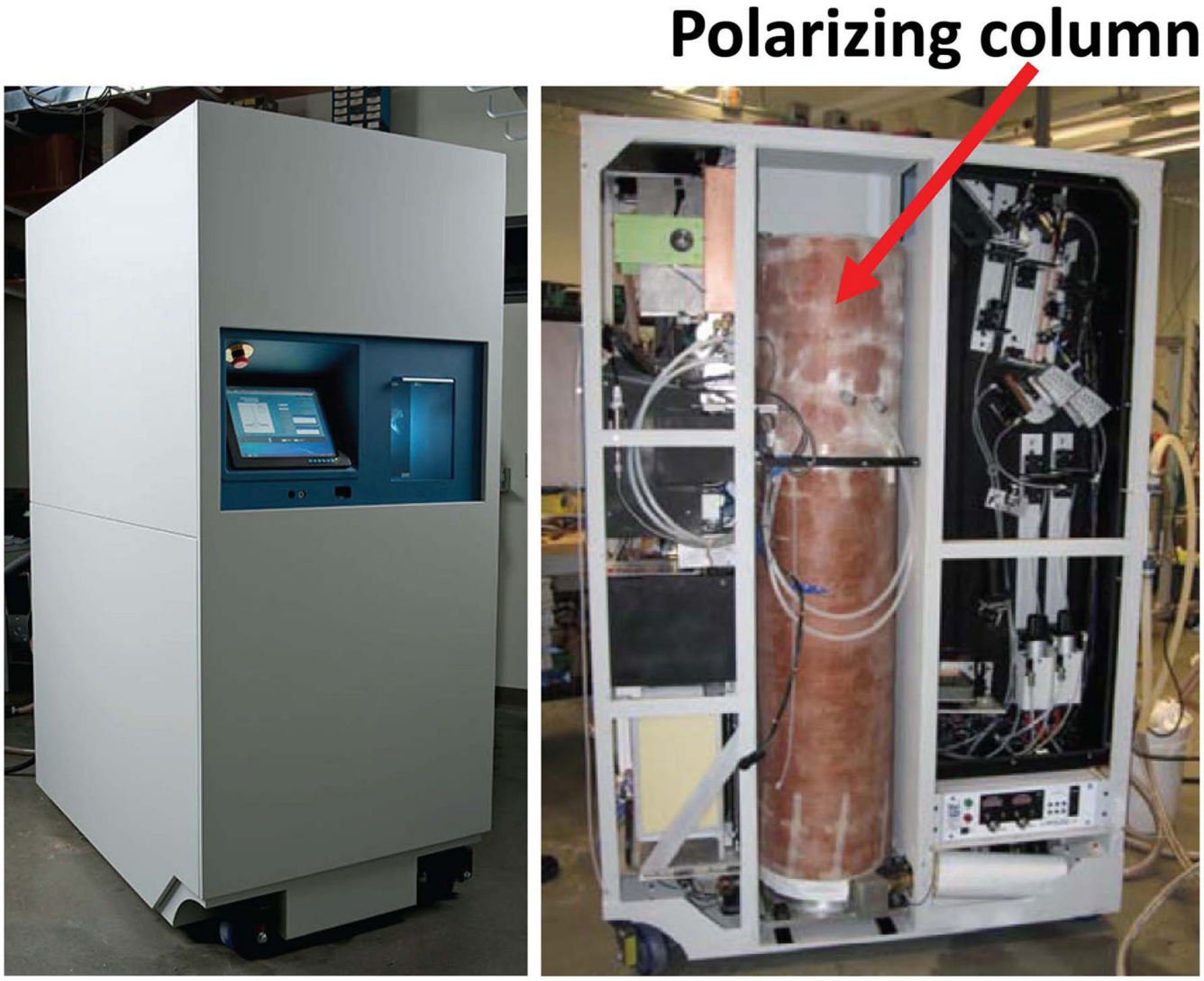

Figure 2.
State-of-the-art gas-polarization system for ^{129}Xe. These photographs show a prototype commercial fourth-generation gas-polarization system optimized for ^{129}Xe (model XeBox-E10, Xemed, LLC, Durham, NH). This polarizer is based on the flowing approach for hyperpolarized-gas production as discussed in the text. The polarizing column, which is the functional analog of the optical cell shown in Fig. 1, is indicated on the right. Additional technical details can be found in ref. (28).

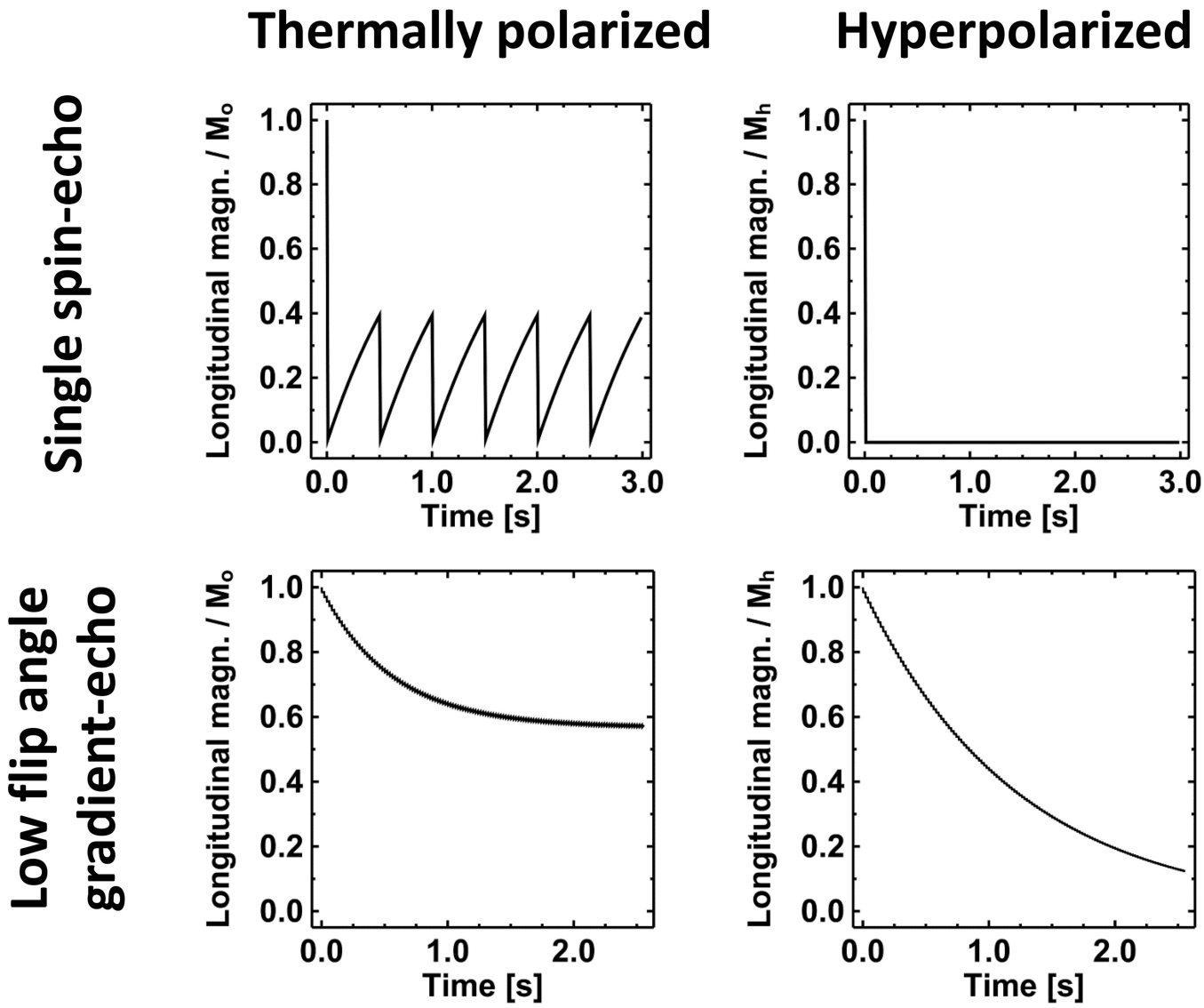

Figure 3.

Effect of T1 relaxation on thermally-polarized versus hyperpolarized magnetization. These plots compare the evolution of the longitudinal component of thermally-polarized magnetization (left column) to that of hyperpolarized magnetization (right column) for the first several repetitions of either a single spin-echo (upper row) or low-flip-angle gradient-echo (lower row) pulse sequence. Due to the non-equilibrium nature of the hyperpolarized magnetization, pulse sequences using repeated, high-flip-angle RF pulses, such as a spin-echo method as illustrated in the upper row, are not useful for hyperpolarized-gas imaging of the lung. In contrast, for appropriate pulse-sequence parameter values, low-flip-angle gradient-echo imaging yields similar relative magnetization evolutions for both thermally-polarized and hyperpolarized magnetization as illustrated in the lower row. For the single spin-echo pulse sequence a 90° excitation RF pulse is applied every 0.5 s (i.e., TR = 500 ms) starting at time zero, and for the low-flip-angle gradient-echo pulse sequence a 10° excitation RF pulse is applied every 20 ms starting at time zero. For thermally-polarized and hyperpolarized magnetization, the T1 values are representative of biological tissue (1 s) and ^{129}Xe in the lung (20 s), respectively, and the initial values of the magnetization are

denoted M_o and M_h, respectively. Ideal spoiling of transverse magnetization between pulse-sequence repetitions is assumed.

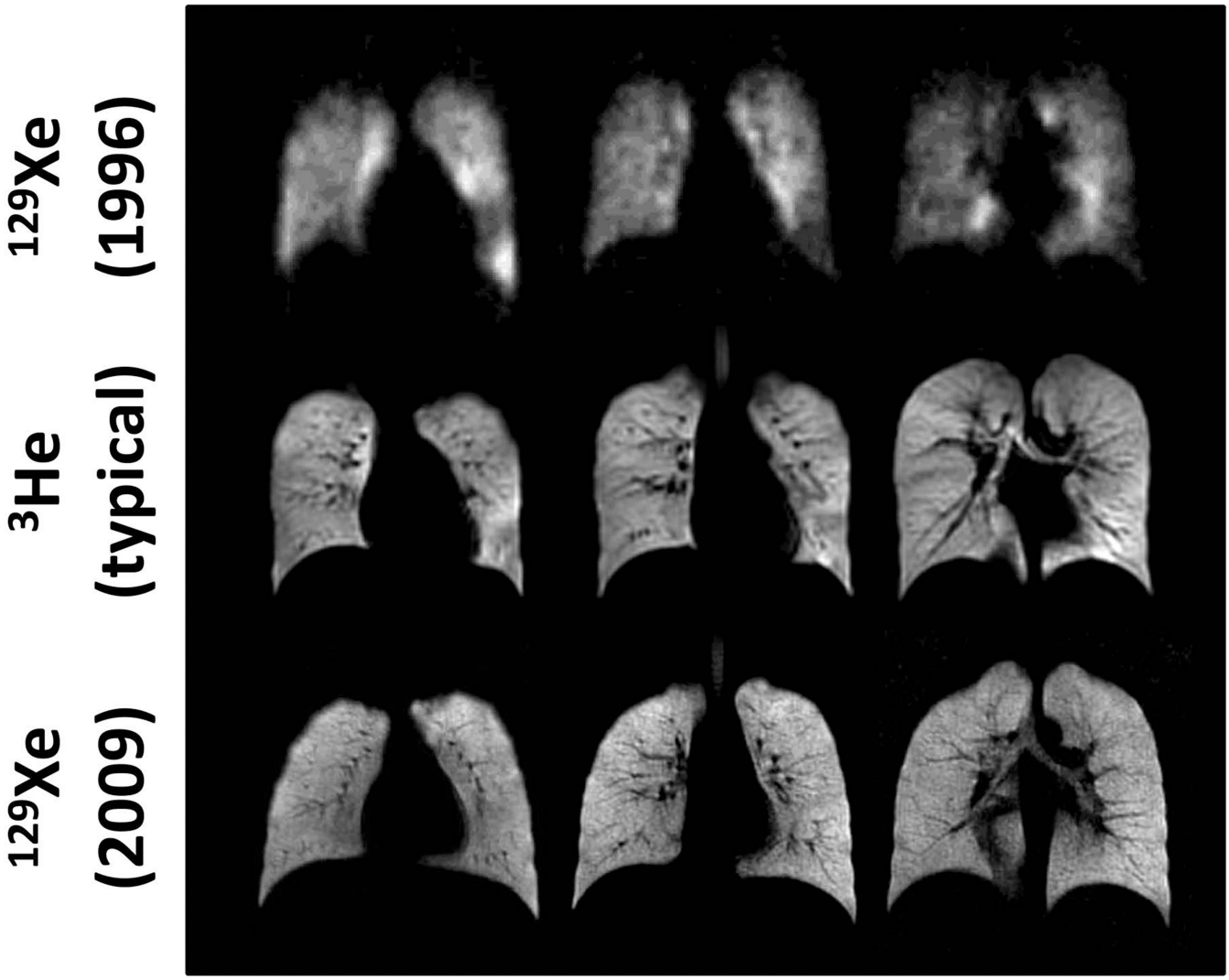

Figure 4.

Ventilation imaging of the healthy human lung. Coronal ventilation images were acquired using hyperpolarized ^{129}Xe (upper and lower rows) or ^{3}He (middle row). In both the ^{3}He images shown in the middle row and the ^{129}Xe images shown in the lower row, hyperpolarized gas distributed generally uniformly throughout the ventilated airspaces of the lung. The tremendous improvement in the quality of ^{129}Xe images between 1996 and 2009 is attributable primarily to an increase in gas polarization; gas polarizations were approximately 1% for the images in the upper row and 35% for those in the middle and lower rows. The images in the upper and middle rows were acquired at 1.5T using a single-channel chest RF coil, while those in the lower row were acquired at 3T using a 32-channel array chest RF coil (33). All images were obtained using a low-flip-angle gradient-echo (FLASH) pulse sequence. (Images in the upper row are reproduced with permission from Fig. 1 of ref. (12), and those in the lower row are from the healthy subject shown in Fig. 1 of ref. (48).)

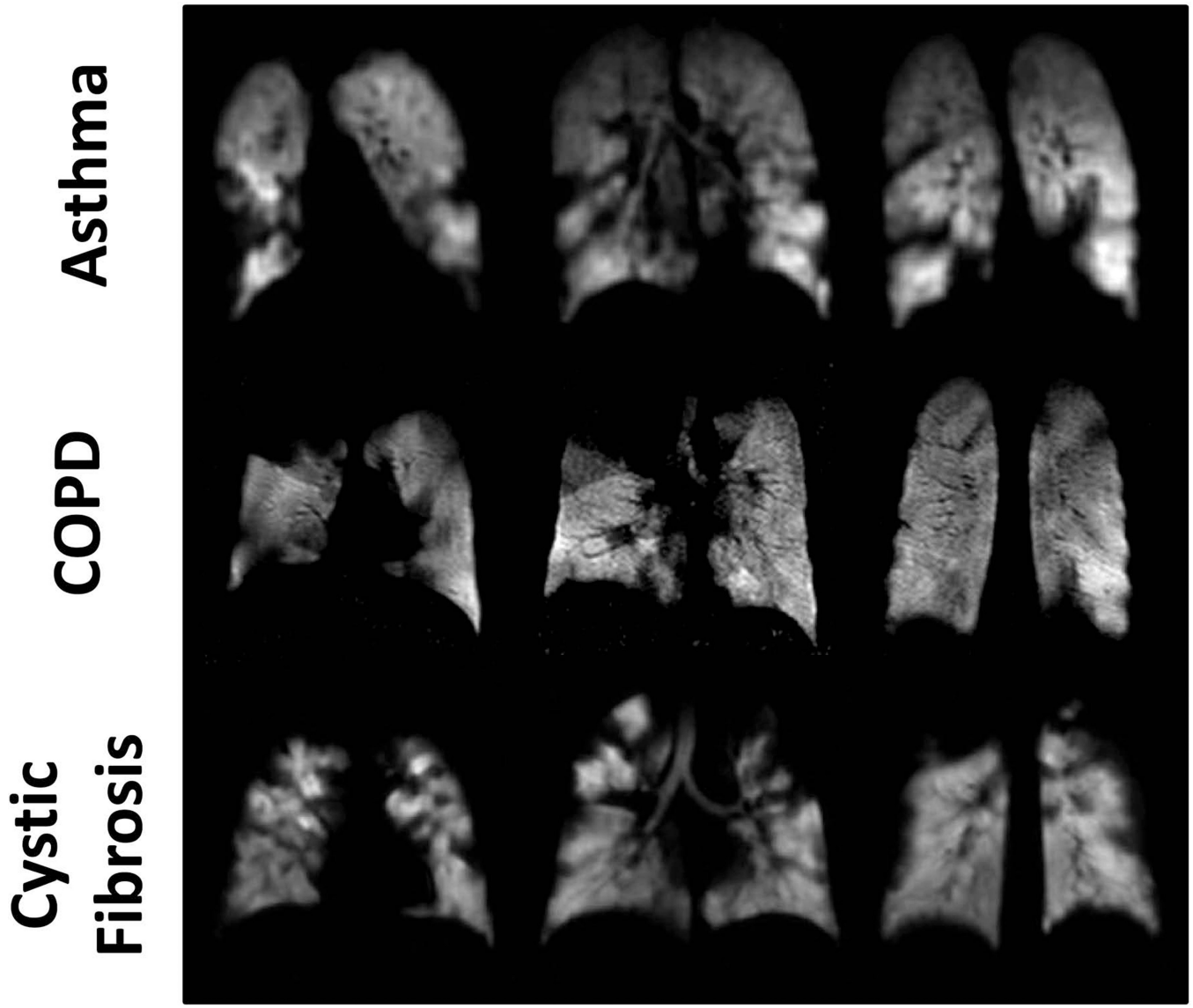

Figure 5.
Ventilation imaging of the diseased human lung using ^{129}Xe. Coronal ventilation images were acquired in subjects with asthma (upper row), COPD (middle row) or cystic fibrosis (lower row). Numerous ventilation defects are seen in each of the images secondary to airflow obstruction caused by the underlying diseases. Gas polarizations were between approximately 25% and 35%. The images in the upper and middle rows were acquired at 3T using a 32-channel array chest RF coil, while those in the lower row were acquired at 1.5T using a single-channel chest RF coil. All images were obtained using a low-flip-angle gradient-echo-based (FLASH or TrueFISP) pulse sequence. (Images in the middle row are from the corresponding subject shown in Fig. 1 of ref. (48). Images in the bottom row are from the same subject shown in the first row of Fig. 1 in ref. (100).)

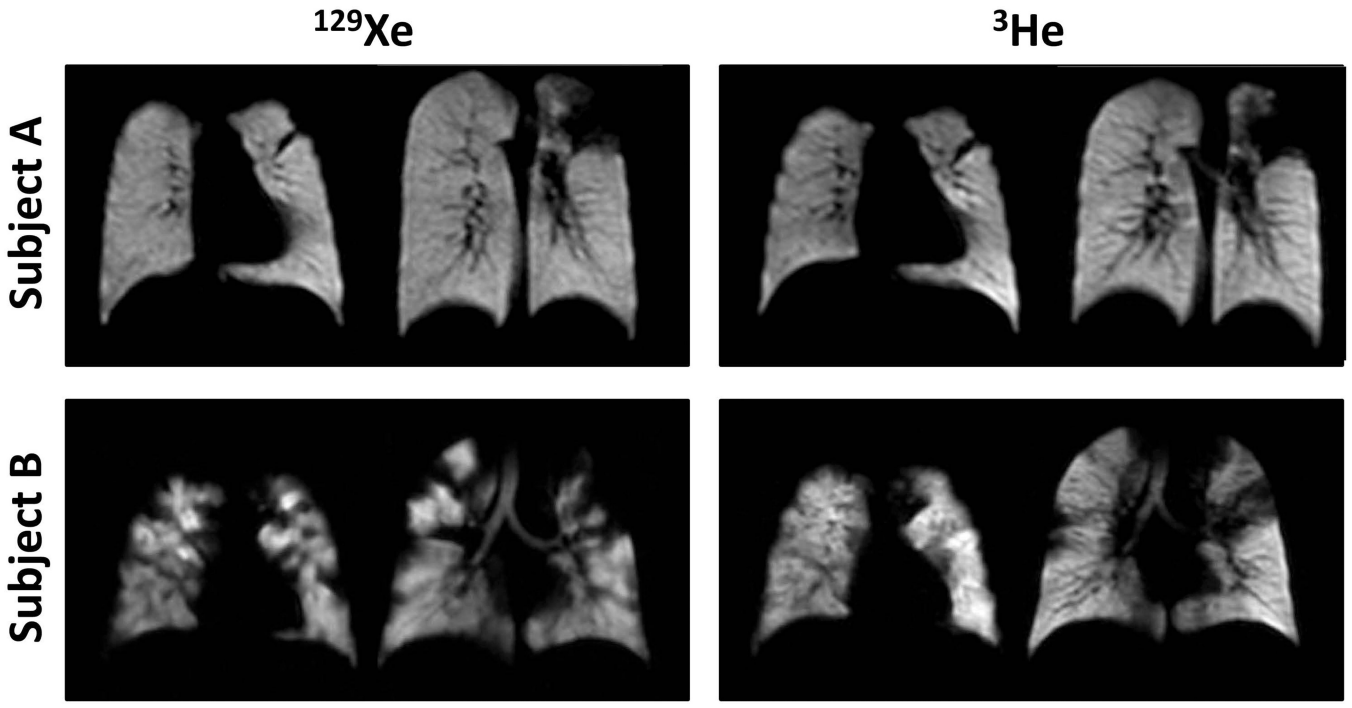

Figure 6.
Comparison of ventilation imaging using ^{129}Xe and ^{3}He in cystic fibrosis. Coronal ventilation images were acquired in two subjects with cystic fibrosis; imaging for each subject was completed on the same day. While, in subject A, the ventilation defects in ^{129}Xe images appear very similar to those in ^{3}He images, in subject B the ventilation defects in ^{129}Xe images appear more severe than those in ^{3}He images. This difference observed in subject B is possibly attributable to the different physical properties of ^{129}Xe and ^{3}He gases. All images were acquired at 1.5T using a single-channel chest RF coil and a low-flip-angle gradient-echo-based (FLASH or TrueFISP) pulse sequence. (Images in the top and bottom rows are from the same subjects shown in the second and first rows, respectively, of Fig. 1 in ref. (100).)

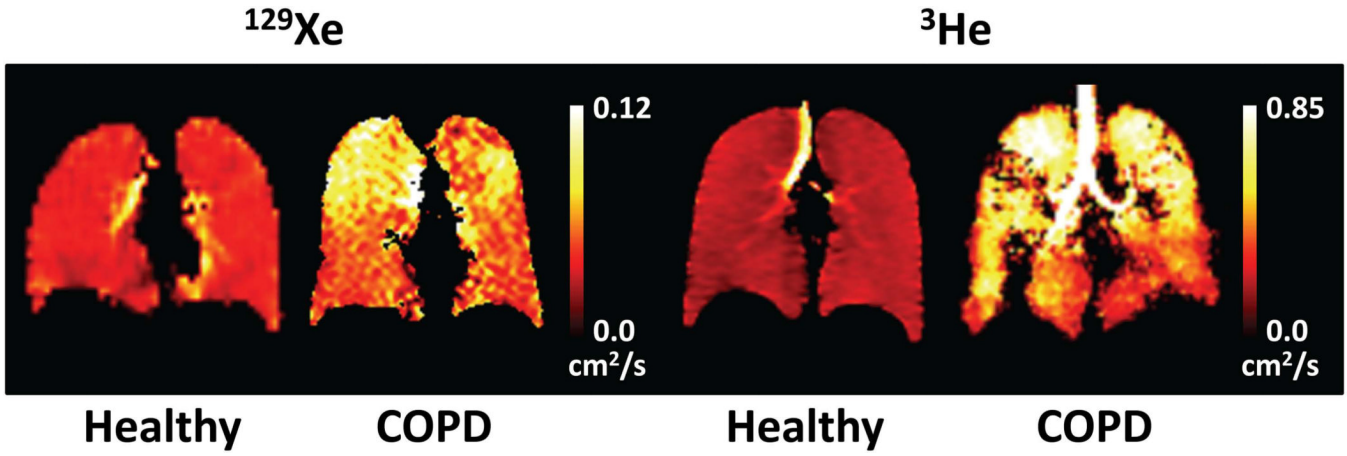

Figure 7.

Comparison of diffusion imaging using ^{129}Xe and ^{3}He. Coronal ADC maps were obtained in two healthy subjects and in two subjects with COPD using ^{129}Xe (left two images) or ^{3}He (right two images). For both gases, the ADC values are relatively low and spatially uniform in the healthy subjects. In contrast, the ADC values for the COPD subjects are markedly inhomogeneous and generally elevated compared to those for the healthy subjects, particularly in the apices. All images were obtained using a low-flip-angle gradient-echo (FLASH) pulse sequence that included a bipolar gradient waveform, applied between the excitation RF pulse and the spatial encoding gradients, to impart diffusion sensitization (*b* values: 0 and 10 s/cm^2 [^{129}Xe] or 0 and 1.6 s/cm^2 [^{3}He]). (^{129}Xe ADC map for COPD is from the same subject shown in Fig. 4 of ref. (91).)

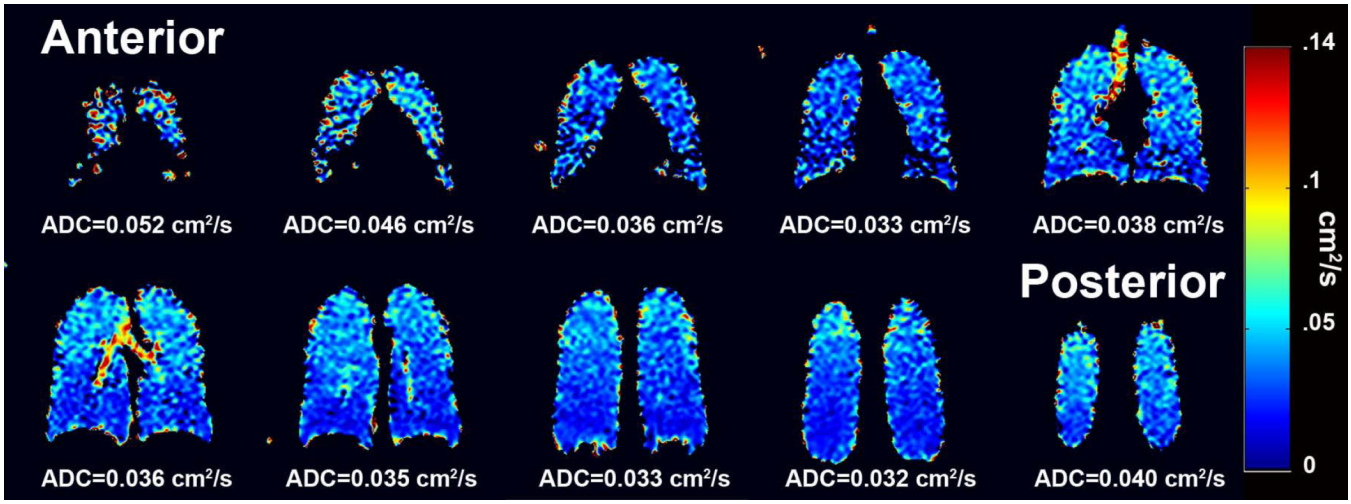

Figure 8.
Directional gradients in ^{129}Xe ADC values. Coronal ADC maps obtained in a healthy subject demonstrate gradients of the ADC values in both the anterior-posterior and superior-inferior directions. The anterior-posterior gradient is attributed to the well-known gravity-dependent gradient in lung tissue density from anterior to posterior in the supine position. Kaushik et al suggest that the superior-inferior gradient may be associated with regional variation in concentration of the inhaled ^{129}Xe (36), although similar variations in ADC values have also been observed using ^{3}He (71). (Fig. 5 from ref. (36), reproduced with permission.)

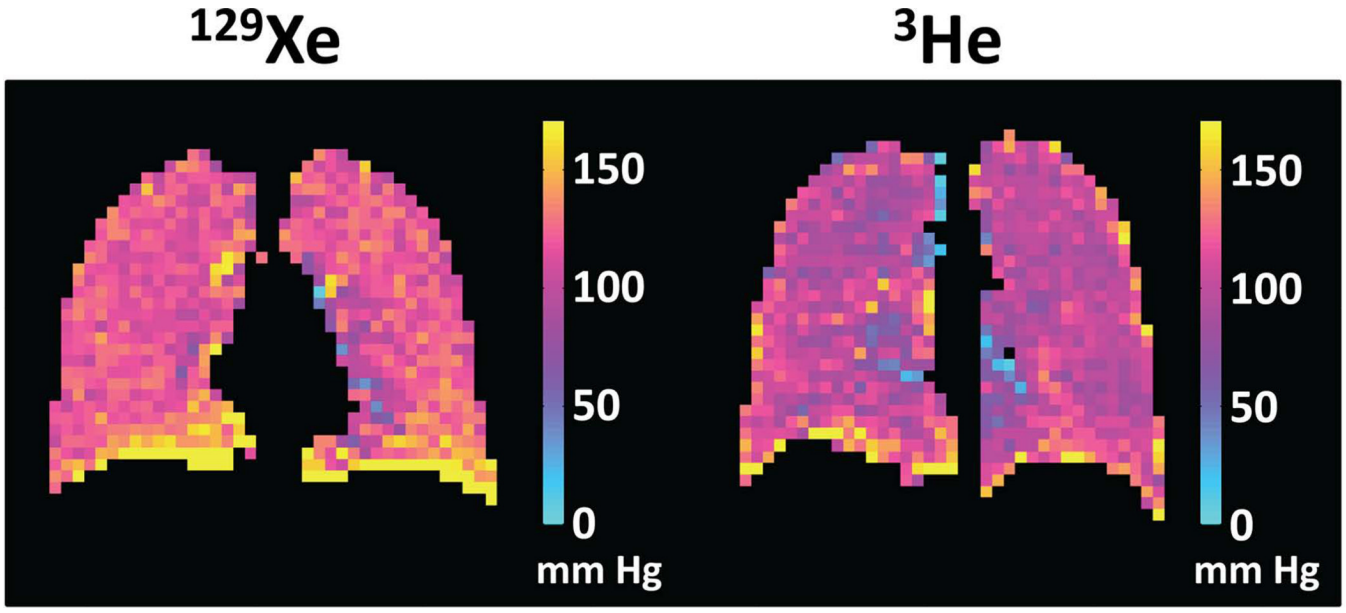

Figure 9.

Comparison of oxygen-concentration imaging using ^{129}Xe and ^{3}He. Coronal maps of the partial pressure of oxygen (pO_2) were obtained in healthy subjects using either ^{129}Xe (left) or ^{3}He (right). For both gases, the pO_2 values are generally uniform and in a range consistent with normal lung physiology, except for artifactually high values at the base of the lung caused by slight motion of the diaphragm during the acquisitions. Both images were obtained using a gradient-echo-based, cardiac-triggered, short-breath-hold implementation of pO_2 mapping (101). (^{129}Xe pO_2 map is from healthy subject #1 in ref. (101).)

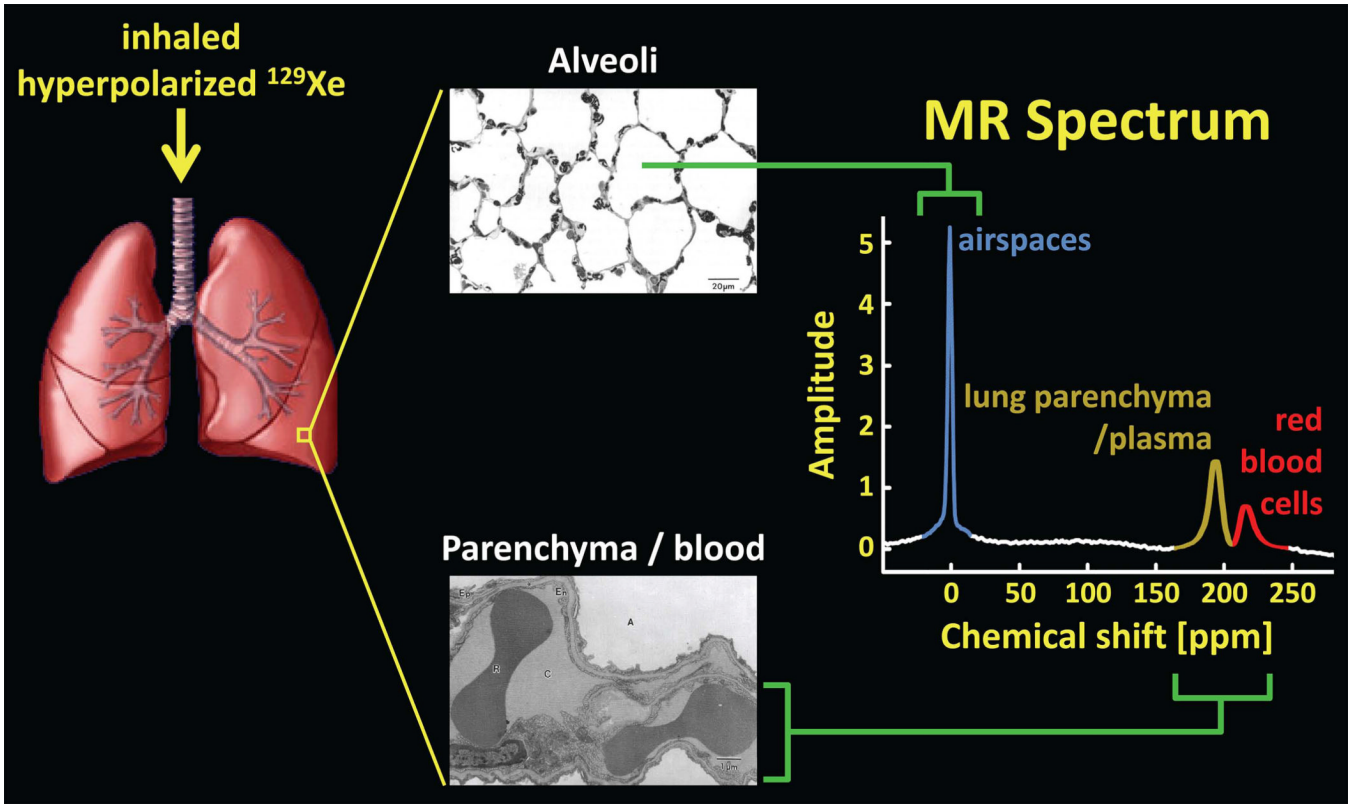

Figure 10.

^{129}Xe in the lung. Inhaled xenon gas distributes among the airspaces of the lung and also dissolves in the lung parenchyma and blood. Because of the large chemical-shift, and hence frequency, difference between ^{129}Xe in the airspaces (alveoli) and that in the parenchyma/blood, an MR spectrum of ^{129}Xe in the lung reveals distinct spectral peaks corresponding to the gas and dissolved components. For clarity, the dissolved-phase peaks, associated with roughly 2% of ^{129}Xe in the lung, are shown several times larger than they would appear if the same flip angle was applied to both the gas-phase and dissolved-phase compartments. (Lung rendering adapted from: dir.niehs.nih.gov/dirlrb/mcb/proj-cox.htm. Micrographs reproduced with permission from Albertine KH. Structural organization and quantitative morphology of the lung. In: Cutillo AG, ed. Application of Magnetic Resonance to the Study of Lung. Hoboken, NJ: Wiley-Blackwell, 1996; 73–114.)

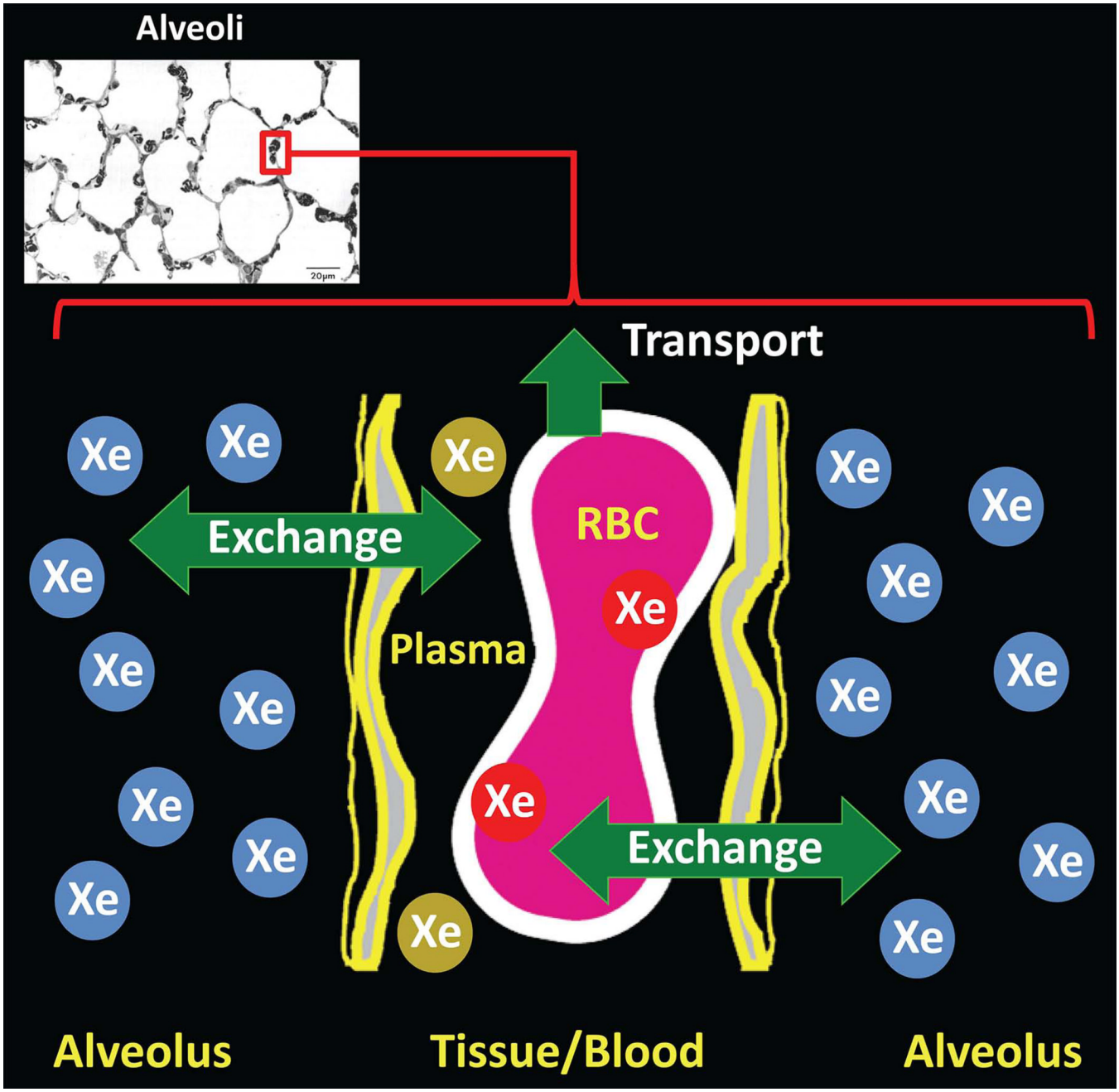

Figure 11.
^{129}Xe exchange between lung airspaces and tissue. Following inhalation, a dynamic equilibrium is quickly established between xenon in the airspaces and xenon dissolved in the parenchyma and blood, resulting in diffusion-driven exchange of xenon between the airspaces (blue Xe atoms) and dissolved-phase compartments (red and gold Xe atoms). A fraction of dissolved xenon is transported to other organs by the bloodstream. (Diagram adapted from Fig. 2 of ref. (20). Micrograph reproduced with permission from Albertine KH. Structural organization and quantitative morphology of the lung. In: Cutillo AG, ed. Application of Magnetic Resonance to the Study of Lung. Hoboken, NJ: Wiley-Blackwell, 1996; 73–114.)

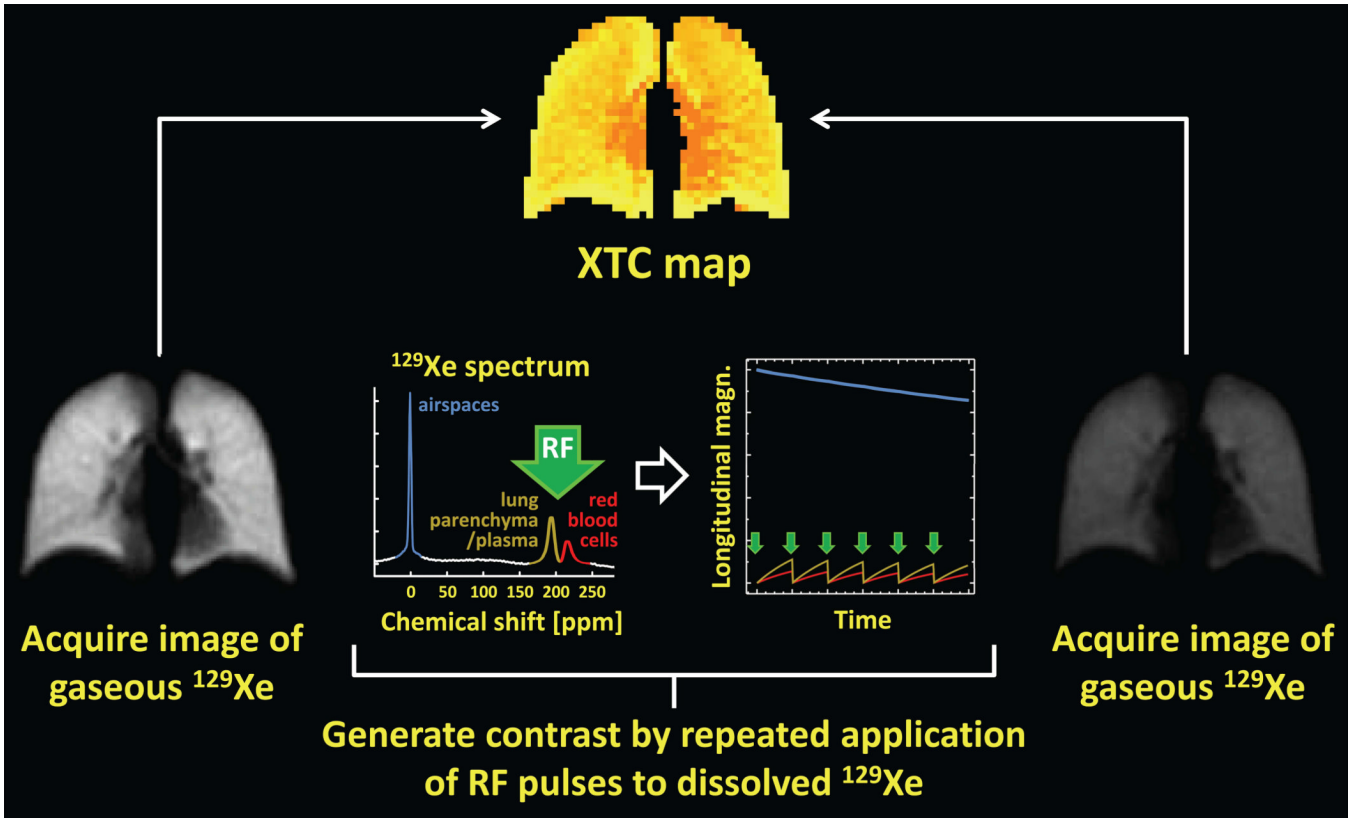

Figure 12.

XTC: Xenon polarization transfer contrast. Following inhalation of hyperpolarized gas, a low-flip-angle, gradient-echo image of gas-phase ^{129}Xe is acquired (left). Next, image contrast reflecting the degree of gas exchange between the airspaces and tissue/blood is generated by applying a series of high-flip-angle RF pulses (green arrows in plots) at the frequency corresponding to the dissolved-phase compartments. During the delay between applications of these contrast-generating high-flip-angle RF pulses, exchange of xenon atoms between the airspaces and tissue/blood causes the gas-phase longitudinal magnetization to decrease (plot on right, blue curve) by an amount proportional to the degree of exchange. Finally, a second low-flip-angle, gradient-echo image of gas-phase ^{129}Xe is acquired (right). Analysis of the changes in signal intensity between the first and second images provides a regional map (top) reflecting the degree of gas exchange that occurred during the delay between contrast-generating RF pulses. For clarity, the dissolved-phase peaks (plot on left) and associated plots of longitudinal magnetization (plot on right) are shown several times larger than actual values.

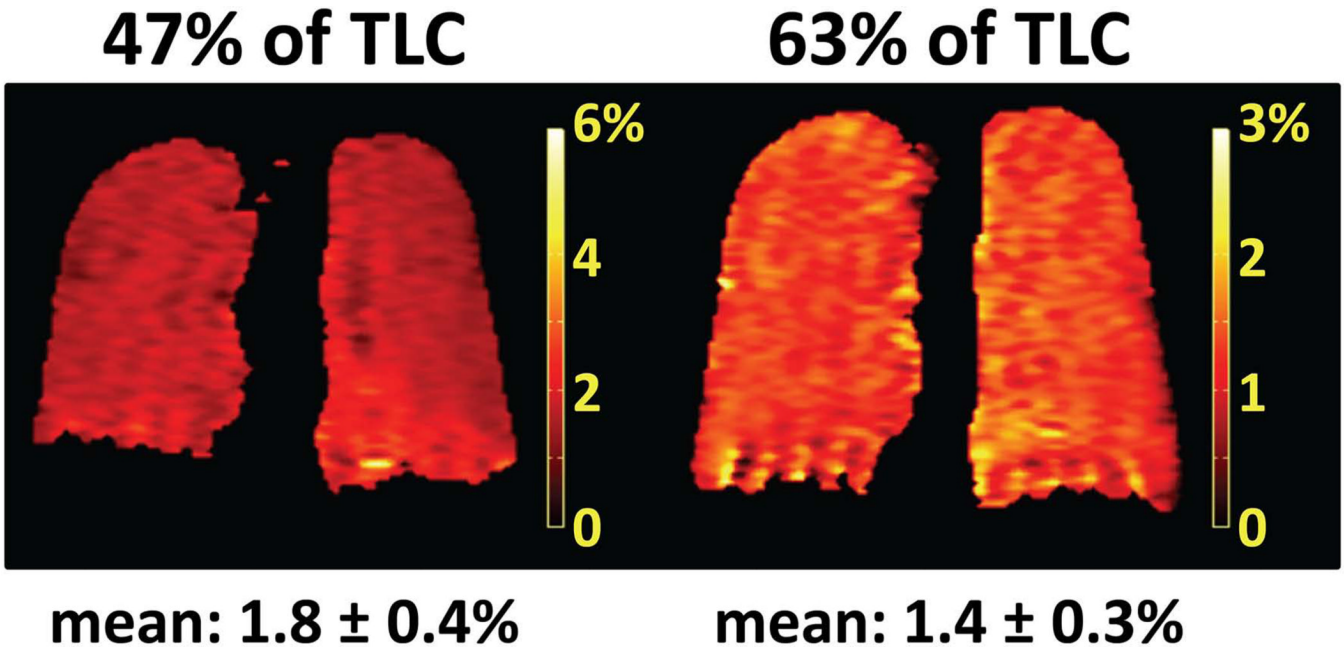

Figure 13.

XTC in a healthy human subject. Maps of fractional gas exchange were calculated from single breath-hold XTC acquisitions at 0.2T (25) performed at 47% (left) and 63% (right) of total lung capacity (TLC) in a healthy volunteer. The mean value of the fractional gas exchange decreased from 1.8% (47% of TLC) to 1.4% (63% of TLC) in response to the increase in lung volume. Although the fractional gas exchange appeared fairly uniform across the lung in both cases, summation of the values along the left-right direction revealed an increase in fractional gas exchange of roughly 0.5% from apex to base for 47% of TLC, whereas the corresponding values for 63% of TLC were uniform from apex to base (25). The time delay between applications of high-flip-angle RF pulses to the dissolved-phase compartments was 62 ms; other acquisition parameters are described in ref. (25). Note that the color scale for the map on the left has a maximum of 6%, while that for the map on the right has a maximum of 3%. (Maps of fractional gas exchange reprinted from European Journal of Radiology, 64(3), Patz S, Hersman FW, Muradian I, et al., Hyperpolarized ^{129}Xe MRI: a viable functional lung imaging modality?, 335–344, Copyright 2007, with permission from Elsevier.)

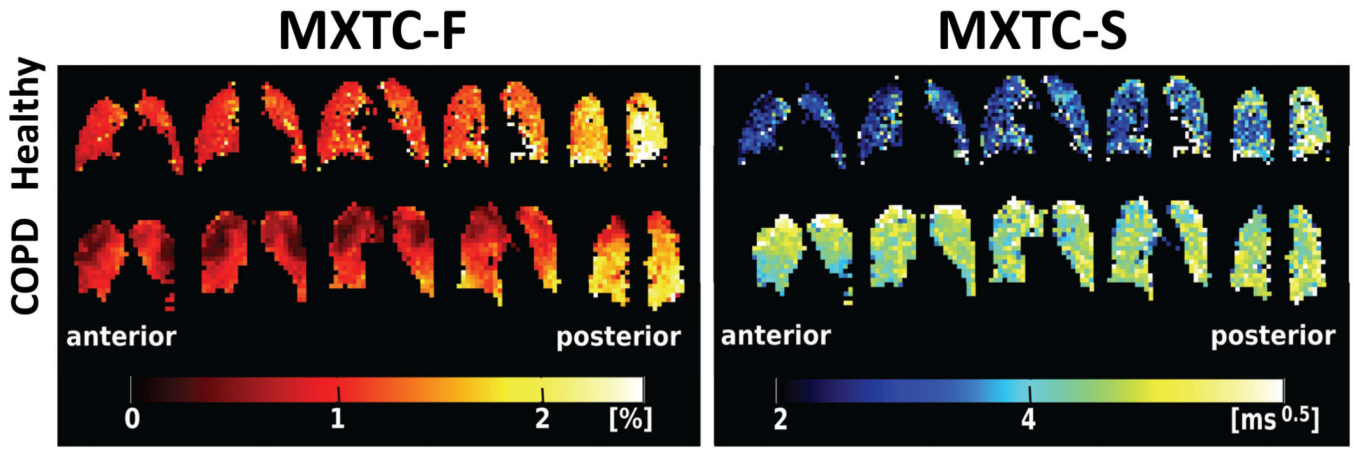

Figure 14.

Lung microstructural parameters from XTC. Maps of the parameters MXTC-F (left half of figure), proportional to the tissue to alveolar-volume ratio, and MXTC-S (right half of figure), proportional to the mean septal wall thickness, were derived from multiple-exchange-time XTC acquisitions at 3T (91). In a healthy volunteer (upper row), both MXTC-F and MXTC-S clearly increased along the anterior-posterior direction, and were either generally uniform or showed relatively small variations within coronal sections. In contrast, for a subject with COPD (lower row), MXTC-F showed marked regional variations within sections with lower values in the apices. Further, MXTC-S did not show substantial variation along the anterior-posterior direction, but was generally higher than for the healthy subject. Acquisition parameters are described in ref. (91). (Maps reproduced with permission from Fig. 2 in ref. (91).)

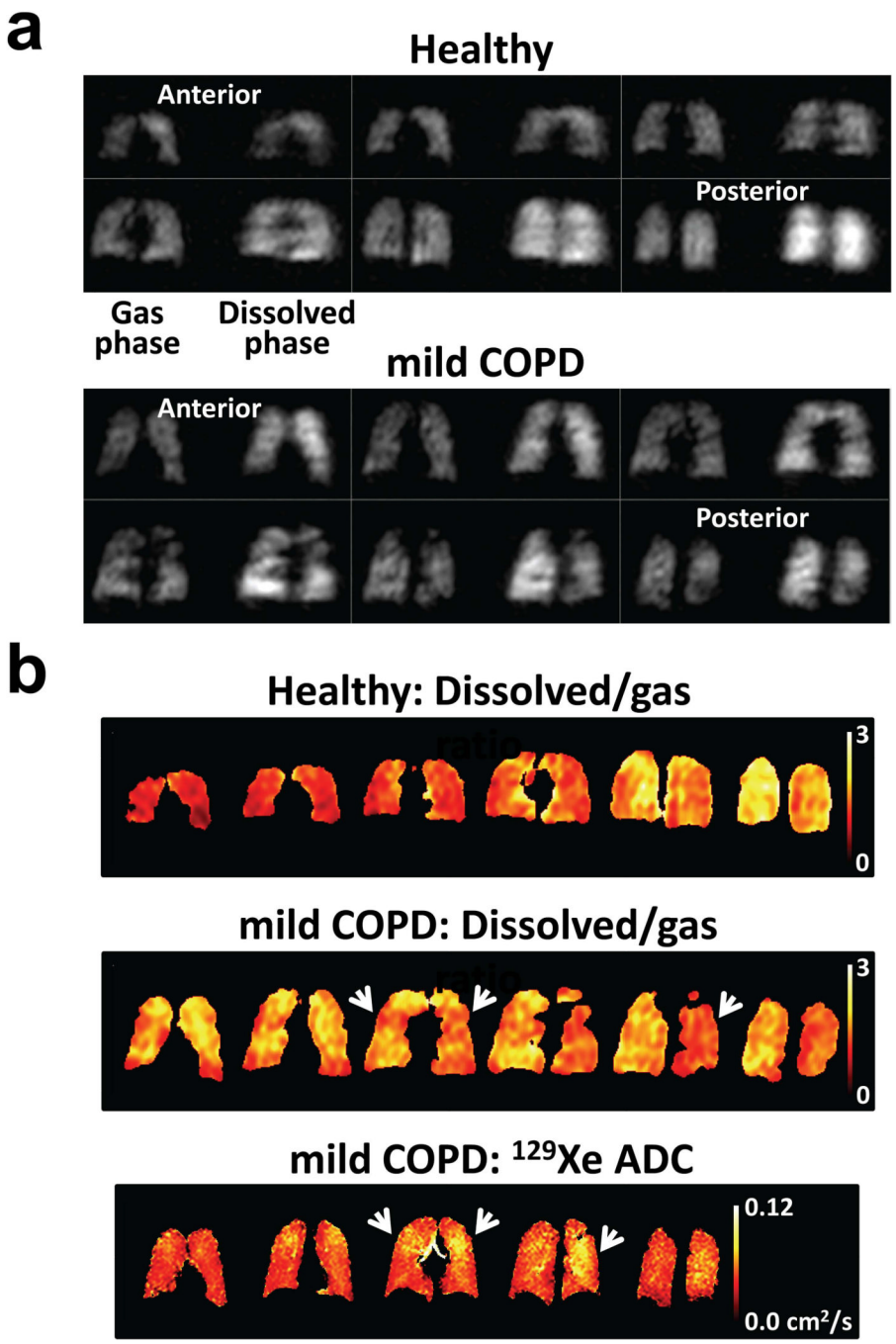

Figure 15.

Direct imaging of dissolved ^{129}Xe in the human lung. (**a**) Three-dimensional acquisitions depicting gas-phase ^{129}Xe in the lung airspaces (left side of each section) and dissolved-phase ^{129}Xe in the tissue and blood (right side of each section) from a healthy subject (top) and a subject with mild (GOLD stage 1) COPD (bottom) (95). While the signal-intensity distributions for the gas-phase and dissolved-phase components were generally uniform for the healthy subject, except for noticeably higher dissolved-phase signal intensity in the posterior portion of the lung, both gas-phase and dissolved-phase components showed non-uniform signal distributions in the subject with COPD, with some regions of mismatch

between corresponding gas-phase and dissolve-phase signal variations. Acquisition parameters are described in ref. (95). (Adapted from Fig. 2 in ref. (95).) (**b**) Maps showing the ratio of dissolved-phase to gas-phase ^{129}Xe in the healthy (top row) and COPD (middle row) subjects, and showing the ADC for ^{129}Xe (b values of 0 and 10 s/cm^2) for the COPD subject (lower row). In the anterior portion of the lung, the ratio of dissolved-phase to gas-phase ^{129}Xe for the COPD subject was substantially higher than that for the healthy subject. Regions of relatively low ratio values for the COPD subject were generally associated with elevated ADC values (e.g., arrowheads).

Table 1

Properties of ^{129}Xe and ^{3}He gases, and protons in water.

Nucleus	Natural abundance [%]	Gyromagnetic ratio [MHz/T]	Diffusion coefficient [cm^2/s]		Ostwald solubility coefficient[2]		
			Pure[1]	Dilute gas in air[2]	Water	Blood	Oil
^{129}Xe	26	−11.8	0.06	0.14	0.083	0.14	1.7
^{3}He	10^{-4}	−32.4	1.8	0.86	0.0098	0.0099	0.018
^{1}H (water)	--	42.6	~2×10^{-5}	--	--	--	--

[1]Data are at 1 atm. and 20°C. “Pure” refers to the self-diffusion coefficient. ^{3}He data from ref. (96); ^{129}Xe data from ref. (97).

[2]Estimated values are at 1 atm. and 37°C (98).

[3]Volume of gas at 1 atm. that dissolves in unit volume of fluid. Data are for 37°C and natural abundance gases (16).

J Magn Reson Imaging. Author manuscript; available in PMC 2014 February 01.